bioRxiv preprint doi: https://doi.org/10.1101/2020.07.11.192948; this version posted November 21, 2020. The copyright holder for this preprint (which was not certified by peer review) is the author/funder. All rights reserved. No reuse allowed without permission.

DIPPER: a spatiotemporal proteomics atlas of human intervertebral discs for exploring ageing and degeneration dynamics

Vivian Tam[1,2*], Peikai Chen[1*], Anita Yee[1], Nestor Solis[3], Theo Klein[3,4], Mateusz Kudelko[1], Rakesh Sharma[5], Wilson CW Chan[1,2,6], Christopher M. Overall[3], Lisbet Haglund[7], Pak C Sham[8], Kathryn SE Cheah[1], Danny Chan[1,2]

[1] School of Biomedical Sciences, The University of Hong Kong, Hong Kong, China;
[2] The University of Hong Kong Shenzhen of Research Institute and Innovation, Shenzhen, China;
[3] Centre for Blood Research, Faculty of Dentistry, University of British Columbia, Vancouver, Canada;
[4] Present address: Triskelion BV, Zeist, The Netherlands;
[5] Proteomics and Metabolomics Core Facility, The University of Hong Kong, Hong Kong, China;
[6] Department of Orthopaedics Surgery and Traumatology, HKU-Shenzhen Hospital, Shenzhen, China;
[7] Department of Surgery, McGill University, Montreal, Canada;
[8] Centre for PanorOmic Sciences (CPOS), The University of Hong Kong, Hong Kong, China.

KSEC is a senior editor at eLife. All other authors declare that they do not have any conflict of interests

* These authors contributed equally to this manuscript

Correspondence should be addressed to:

Danny Chan
School of Biomedical Sciences
Faculty of Medicine
The University of Hong Kong
21 Sassoon Road, Hong Kong
Email: chand@hku.hk
Tel.: +852 3917 9482

bioRxiv preprint doi: https://doi.org/10.1101/2020.07.11.192948; this version posted November 21, 2020. The copyright holder for this preprint (which was not certified by peer review) is the author/funder. All rights reserved. No reuse allowed without permission.

Abstract

The spatiotemporal proteome of the intervertebral disc (IVD) underpins its integrity and function. We present DIPPER, a deep and comprehensive IVD proteomic resource comprising 94 genome-wide profiles from 17 individuals. To begin with, protein modules defining key directional trends spanning the lateral and anteroposterior axes were derived from high-resolution spatial proteomes of intact young cadaveric lumbar IVDs. They revealed novel region-specific profiles of regulatory activities, and displayed potential paths of deconstruction in the level- and location-matched aged cadaveric discs. Machine learning methods predicted a "hydration matrisome" that connects extracellular matrix with MRI intensity. Importantly, the static proteome used as point-references can be integrated with dynamic proteome (SILAC/degradome) and transcriptome data from multiple clinical samples, enhancing robustness and clinical relevance. The data, findings and methodology, available on a web interface, will be valuable references in the field of IVD biology and proteomic analytics.

(142 words)

Key words: human, intervertebral discs, nucleus pulposus, annulus fibrosus, ageing, extracellular matrix, proteomics, TAILS, degradome, SILAC, transcriptomics

bioRxiv preprint doi: https://doi.org/10.1101/2020.07.11.192948; this version posted November 21, 2020. The copyright holder for this preprint (which was not certified by peer review) is the author/funder. All rights reserved. No reuse allowed without permission.

Introduction

The 23 intervertebral discs (IVDs) in the human spine provide stability, mobility and flexibility. IVD degeneration (IDD), most common in the lumbar region (Saleem et al., 2013; Teraguchi et al., 2014), is associated with a decline in function and a major cause of back pain, affecting up to 80% of the world's population at some point in life (Rubin, 2007), presenting significant socioeconomic burdens. Multiple interacting factors such as genetics, influenced by ageing, mechanical and other stress factors, contribute to the pathobiology, onset, severity and progression of IDD (Munir et al., 2018).

IVDs are large, avascular, extracellular matrix (ECM)-rich structures comprising three compartments: a hydrated nucleus pulposus (NP) at the centre, surrounded by a tough annulus fibrosus (AF) at the periphery, and cartilaginous endplates of the adjoining vertebral bodies (Humzah and Soames, 1988). The early adolescent NP is populated with vacuolated notochordal-like cells, which are gradually replaced by small chondrocyte-like cells (Risbud et al., 2015). Blood vessels terminate at the endplates, nourishing and oxygenating the NP via diffusion, whose limited capacity mean that NP cells are constantly subject to hypoxic, metabolic and mechanical stresses (Urban et al., 2004).

With ageing and degeneration, there is an overall decline in cell "health" and numbers (Rodriguez et al., 2011; Sakai et al., 2012), disrupting homeostasis of the disc proteome. The ECM has key roles in biomechanical function and disc hydration. Indeed, a hallmark of IDD is reduced hydration in the NP, diminishing the disc's capacity to dissipate mechanical loads. Clinically, T-2 weighted magnetic resonance imaging (MRI) is the gold standard for assessing IDD, that uses disc hydration and structural features such as bulging or annular tears to measure severity (Pfirrmann et al., 2001; Schneiderman et al., 1987). The hydration and mechanical properties of the IVD are dictated by the ECM composition, which is produced and maintained by the IVD cells.

To meet specific biomechanical needs, cells in the IVD compartments synthesise different compositions of ECM proteins. Defined as the "matrisome" (Naba et al., 2012), the ECM houses the cells and facilitates their inter-communication by regulation of the availability and presentation of signalling molecules (Taha and Naba, 2019). With ageing or degeneration, the NP becomes more fibrotic and less compliant (Yee et al., 2016), ultimately affecting disc biomechanics (Newell

bioRxiv preprint doi: https://doi.org/10.1101/2020.07.11.192948; this version posted November 21, 2020. The copyright holder for this preprint (which was not certified by peer review) is the author/funder. All rights reserved. No reuse allowed without permission.

et al., 2017). Changes in matrix stiffness can have a profound impact on cell-matrix interactions and downstream transcriptional regulation, signalling activity and cell fate (Park et al., 2011).

The resulting alterations in the matrisome lead to vicious feedback cycles that reinforce cellular degeneration and ECM changes. Notably, many of the associated IDD genetic risk factors, such as COL9A1 (Jim et al., 2005), ASPN (Song et al., 2008), and CHST3 (Song et al., 2013), are variants in genes encoding matrisome proteins, highlighting their importance for disc function. Therefore, knowledge of the cellular and extracellular proteome and their spatial distribution in the IVD is crucial to understanding the mechanisms underlying the onset and progression of IDD (Feng et al., 2006).

Current knowledge of IVD biology is inferred from a limited number of transcriptomic studies on human (Minogue et al., 2010; Riester et al., 2018; Rutges et al., 2010) and animal (Veras et al., 2020) discs. Studies showed that cells in young healthy NP express markers including CD24, KRT8, KRT19 and T (Fujita et al., 2005; Minogue et al., 2010; Rutges et al., 2010), whilst NP cells in aged or degenerated discs have different and variable molecular signatures (Chen et al., 2006; Rodrigues-Pinto et al., 2016), such as genes involved in TGFβ signalling (TGFA, INHA, INHBA, BMP2/6). The healthy AF expresses genes including collagens (COL1A1 and COL12A1) (van den Akker et al., 2017), growth factors (PDGFB, FGF9, VEGFC) and signalling molecules (NOTCH and WNT) (Riester et al., 2018). Although transcriptomic data provides valuable cellular information, it does not faithfully reflect the molecular composition. Cells represent only a small fraction of the disc volume, transcriptome-proteome discordance does not enable accurate predictions of protein levels from mRNA (Fortelny et al., 2017), and the disc matrisome accumulates and remodels over time.

Proteomic studies on animal models of IDD, including murine (McCann et al., 2015), canine (Erwin et al., 2015), and bovine (Caldeira et al., 2017), have been reported. Nevertheless, human-animal differences in cellular phenotypes and mechanical loading physiologies mean that these findings might not translate to the human scenario. So far, human proteomic studies have compared IVDs with other cartilaginous tissues (Onnerfjord et al., 2012a); and have shown increases in fibrotic changes in ageing and degeneration (Yee et al., 2016), a role for inflammation in degenerated discs (Rajasekaran et al., 2020), the presence of haemoglobins and

bioRxiv preprint doi: https://doi.org/10.1101/2020.07.11.192948; this version posted November 21, 2020. The copyright holder for this preprint (which was not certified by peer review) is the author/funder. All rights reserved. No reuse allowed without permission.

immunoglobulins in discs with spondylolisthesis and herniation (Maseda et al., 2016), and changes in proteins related to cell adhesion and migration in IDD (Sarath Babu et al., 2016). The reported human disc proteomes were limited in the numbers of proteins identified and finer compartmentalisation within the IVD, and disc levels along the lumbar spine have yet to be studied. Nor have the proteome dynamics in term of ECM remodelling (synthesis and degradation) in young human IVDs and changes in ageing and degeneration been described.

In this study, we presented DIPPER (analogous to the Big Dipper which are point-reference stars for guiding nautical voyages), a comprehensive disc proteomic resource, comprising static spatial proteome, dynamic proteome and transcriptome and a methodological flow, for studying the human intervertebral disc in youth, ageing and degeneration. First, we established a high-resolution point-reference map of static spatial proteomes along the lateral and anteroposterior directions of IVDs at three lumbar levels, contributed by a young (16M) and an aged (59M) cadavers with no reported scoliosis or degeneration. We evaluated variations among the disc compartments and levels by principal component analysis (PCA), analysis of variance (ANOVA) and identification of differentially expressed proteins (DEPs). We discovered modules containing specific sets of proteins that describe the directional trends of a young IVD, and the deconstruction of these modules with ageing and degeneration. Using a LASSO regression model, we identified proteins (the hydration matrisome) predictive of tissue hydration as indicated by high-resolution MRI of the aged discs. Finally, we showed how the point-reference proteomes can be utilized, to integrate with other independent transcriptome and dynamic proteome (SILAC and degradome) datasets from additional 15 clinical disc specimens, elevating the robustness of the proteomic findings. An explorable web interface hosting the data and findings is presented, serving as a useful resource for the scientific community.

bioRxiv preprint doi: https://doi.org/10.1101/2020.07.11.192948; this version posted November 21, 2020. The copyright holder for this preprint (which was not certified by peer review) is the author/funder. All rights reserved. No reuse allowed without permission.

Results

Disc samples and their phenotypes

DIPPER comprises 94 genome-wide measurements from lumbar disc components of 17 individuals (Figure 1A; Table 1), with data types ranging from label-free proteomic, transcriptomic, SILAC to degradome (Lopez-Otin and Overall, 2002). High-resolution static spatial proteomes were generated from multiple intact disc segments of young trauma-induced (16 M) and aged (57 M) cadaveric spines. T1- and T2-weighted MRI (3T) showed the young discs (L3/4, L4/5, L5/S1) were non-degenerated, with a Schneiderman score of 1 from T2 images (Figure 1B). The NP of young IVD were well hydrated (white) with no disc bulging, endplate changes, or observable inter-level variations (Figure 1B; Supplemental Figure S1A), consistent with healthy discs and were deemed fit to serve as a benchmarking point-reference. To investigate structural changes associated with ageing, high resolution (7T) MRI was taken for the aged discs (Figure 1C). All discs had irregular endplates, and annular tears were present (green arrowheads) adjacent to the lower endplate and extending towards the posterior region at L3/4 and L4/5 (Figure 1C). The NP exhibited regional variations in hydration in both sagittal and transverse images (Figure 1C). Morphologically, the aged discs were less hydrated and the NP and AF structures less distinct, consistent with gross observations (Supplemental Figure S1A). Scoliosis was not detected in these two individuals.

Information of the disc samples used in the generation of other profiling data are described in methods and Table 1. They are clinical samples taken from patients undergoing surgery. The disc levels and intactness varied, and thus are more suitable for cross-validation purposes and some are directly relevant to IDD.

Quality data detecting large numbers of matrisome and non-matrisome proteins

The intact discs from the two cadaveric spines enabled us to derive spatial proteomes for young and aged human IVDs. We subdivided each lumbar disc into 11 key regions (Figure 1D), spanning the outer-most (outer AF; OAF) to the central-most (NP) region of the disc, traversing both anteroposterior and lateral axes, adding valuable spatial information to our proteomic dataset. Since the disc is an oval shape, an inner AF (IAF) region was assigned in the lateral directions. A

bioRxiv preprint doi: https://doi.org/10.1101/2020.07.11.192948; this version posted November 21, 2020. The copyright holder for this preprint (which was not certified by peer review) is the author/funder. All rights reserved. No reuse allowed without permission.

"mixed" compartment between the NP and IAF with undefined boundary was designated as the NP/IAF in all four (anteroposterior and lateral) directions. In all, this amounted to 66 specimens with different compartments, ages, directions and levels, which then underwent LC-MS/MS profiling (Supplemental Table S1). Systematic analyses of the 66 profiles are depicted in a flowchart (Figure 1A).

A median of 654 proteins per profile were identified for the young samples and 829 proteins for the aged samples, with a median of 742 proteins per profile for young and aged combined. The proteome-wide distributions were on similar scales across the profiles (Supplemental Figure S1B). Of the 3,100 proteins detected in total, 418 were matrisome proteins (40.7% of all known matrisome proteins) and 2,682 non-matrisome proteins (~14% of genome-wide non-matrisome genes) (Figure 1E; Supplemental Figure S1C), and 983 were common to all four major compartments, namely the OAF, IAF, NP/IAF, and NP (Figure 1E, upper panel). A total of 1,883 proteins were identified in young discs, of which 690 (36%) were common to all regions. Additionally, 45 proteins (2.4%) were unique to NP, whilst NP/IAF, IAF and OAF had 86 (4.6%), 54 (2.9%) and 536 (28%) unique proteins, respectively (Figure 1E, middle panel). For the aged discs, 2,791 proteins were identified, of which 803 (28.8%) were common to all regions. NP, NP/IAF and IAF had 34 (12%), 80 (28.7%) and 44 (15%) unique proteins, respectively, with the OAF accounting for the highest proportion of 1,314 unique proteins (47%) (Figure 1E, lower panel). The aged OAF had the highest number of detected proteins with an average of 1,156, followed by the young OAF with an average of 818 (Figure 1F). The quantity and spectrum of protein categories identified suggest sufficient proteins had been extracted and the data are of high quality.

Levels of matrisome proteins decline in all compartments of aged discs

We divided the detected matrisome proteins into core matrisome (ECM proteins, encompassing collagens, proteoglycans and glycoproteins), and non-core matrisome (ECM regulators, ECM affiliated and secreted factors), according to a matrisome classification database (Naba et al., 2012) (matrisomeproject.mit.edu) (Figure 1F). Despite the large range of total numbers of proteins detected (419 to 1,920) across the 66 profiles (Figure 1F), all six sub-categories of the matrisome contained similar numbers of ECM proteins (Figure 1F & G; Supplemental Figure S2A). The non-

bioRxiv preprint doi: https://doi.org/10.1101/2020.07.11.192948; this version posted November 21, 2020. The copyright holder for this preprint (which was not certified by peer review) is the author/funder. All rights reserved. No reuse allowed without permission.

core matrisome proteins were significantly more abundant in aged than in young discs (Supplemental Figure S2A). On average, 19 collagens, 18 proteoglycans, 68 glycoproteins, 52 ECM regulators, 22 ECM affiliated proteins, and 29 secreted factors of ECM were detected per profile. The majority of the proteins in these matrisome categories were detected in all disc compartments, and in both age groups. A summary of all the comparisons are presented in Supplemental Figure S1C-E, and the commonly expressed matrisome proteins are listed in Table 2.

Even though there are approximately three times more non-matrisome than matrisome proteins per profile on average (Figure 1F), their expression levels in terms of label-free quantification (LFQ) values are markedly lower (Supplemental Figure S2B). Specifically, the expression levels of core-matrisome were the highest, with an average $\log_2$(LFQ) of 30.65, followed by non-core matrisome at 28.56, and then non-matrisome at 27.28 (Supplemental Figure S2B). Within the core-matrisome, the expression was higher ($p=6.4\times10^{-21}$) in young (median 30.74) than aged (median 29.72) discs (Supplemental Figure S2C & D). This difference between young and aged discs is consistent within the sub-categories of core and non-core matrisome, with the exception of the ECM regulator category (Figure 1H). The non-core matrisome and non-matrisome, however, exhibited smaller cross-compartment and cross-age differences in terms of expression levels (Supplemental Figure S2E-H). That is, the levels of ECM proteins in each compartment of the disc declines with ageing and possibly changes in the relative composition, while the numbers of proteins detected per matrisome sub-category remain similar. This agrees with the concept that with ageing, ECM synthesis is not sufficient to counterbalance degradation, as exemplified in a proteoglycan study (Silagi et al., 2018).

Cellular activities inferred from non-matrisome proteins

Although 86.5% (2,682) of the detected proteins were non-matrisome, their expression levels were considerably lower than matrisome proteins across all sample profiles (Figure 1F). A functional categorisation according to the Human Genome Nomenclature Committee gene family annotations (Yates et al., 2017) showed many categories containing information for cellular components and activities, with the top 30 listed in Figure 1I. These included transcriptional and translational machineries, post-translational modifications, mitochondrial function, protein turnover; and

bioRxiv preprint doi: https://doi.org/10.1101/2020.07.11.192948; this version posted November 21, 2020. The copyright holder for this preprint (which was not certified by peer review) is the author/funder. All rights reserved. No reuse allowed without permission.

importantly, transcriptional factors, cell surface markers, and inflammatory proteins that can inform gene regulation, cell identity and response in the context of IVD homeostasis, ageing and degeneration.

These functional overviews highlighted 77 DNA-binding proteins and/or transcription factors, 83 cell surface markers, and 175 inflammatory-related proteins, with their clustering data presented as heatmaps (Supplemental Figure S3). Transcription factors and cell surface markers are detected in some profiles (Supplemental Figure S3A and B). The heatmap of the inflammatory-related proteins showed that more than half of the proteins are detected in the majority of samples, with 4 major clusters distinguished by age and expression levels (Supplemental S3C). For example, one of the clusters in the aged samples showed enrichment for complement and coagulation cascades (False Discovery Rate, FDR $q=1.62\times10^{-21}$) and clotting factors (FDR $q=6.05\times10^{-9}$), indicating potential infiltration of blood vessels. Lastly, there are 371 proteins involved in signalling pathways, and their detection frequency in the different compartments and heat map expression levels are illustrated in Supplemental Figure S3D.

Histones and housekeeping genes inform cross compartment- and age-specific variations in cellularity

Cellularity within the IVD, especially the NP, decreases with age and degeneration (Rodriguez et al., 2011; Sakai et al., 2012). We assessed whether cellularity of the different compartments could be inferred from the proteomic data. Quantitation of histones can reflect the relative cellular content of tissues (Wisniewski et al., 2014). We detected 10 histones, including subunits of histone 1 (HIST1H1B/C/D/E, HIST1H2BL, HIST1H3A, HIST1H4A) and histone 2 (HIST2H2AC, HIST2H2BE, HIST2H3A), with 4 subunits identified in over 60 sample profiles that are mutually co-expressed (Supplemental Figure S4A). Interestingly, histone concentrations, and thus cellularity, increased from the inner to the outer compartments of the disc, and showed a highly significant decrease in aged discs compared to young discs across all compartments (Figure 1J), (Wilcoxon $p=5.6\times10^{-4}$) (Supplemental Figure S4B).

GAPDH and ACTA2 are two commonly used reference proteins, involved in the metabolic process and the cytoskeletal organisation of cells, respectively. They are expected to be relatively constant between cells and are used to quantify the relative cellular content of tissues (Barber et

bioRxiv preprint doi: https://doi.org/10.1101/2020.07.11.192948; this version posted November 21, 2020. The copyright holder for this preprint (which was not certified by peer review) is the author/funder. All rights reserved. No reuse allowed without permission.

al., 2005). They were detected in all 66 profiles. GAPDH and ACTA2 amounts were significantly correlated with a Pearson correlation coefficient (PCC) of 0.794 ($p=9.3\times10^{-9}$) (Supplemental Figure S4C), and they were both significantly co-expressed with the detected histone subunits, with PCCs of 0.785 and 0.636, respectively (Figure 1K; Supplemental Figure S4D). As expected, expression of the histones, GAPDH and ACTA2 was not correlated with two core-matrisome proteins, ACAN and COL2A1 (Supplemental Figure S4E); whereas ACAN and COL2A1 were significantly co-expressed (Supplemental Figure S4F), as expected due to their related regulation of expression and tissue function. Thus, cellularity information can be obtained from proteomic information, and the histone quantification showing reduced cellularity in the aged IVD is consistent with the reported changes (Rodriguez et al., 2011; Sakai et al., 2012).

Phenotypic variations revealed by PCA and ANOVA

PCA captures the information content distinguishing age and tissue types

To gain a global overview of the data, we performed PCA on a set of 507 proteins selected computationally, allowing maximal capture of valid values, while incurring minimal missing values, followed by imputations (Supplemental Figure S5; Methods). The first two principal components (PCs) explained a combined 65.5% of the variance, with 39.9% and 25.6% for the first and second PCs, respectively (Figure 2A and B). A support vector machine with polynomial kernel was trained to predict the boundaries: it showed PC1 to be most informative to predict age, with a clear demarcation between the two age groups (Figure 2A, vertical boundary), whereas PC2 distinguished disc sample localities, separating the inner compartments (NP, NP/IAF and IAF) from the OAF (Figure 2A, horizontal boundary). PC3 captured only 5.0% of the variance (Figure 2C & D), but it distinguished disc level, separating the lowest level (L5/S1) from the rest of the lumbar discs (L3/4 and L4/5) (Figure 2D, horizontal boundary). Samples in the upper level (L3/4 and L4/5) appeared to be more divergent, with the aged disc samples deviating from the young ones (Figure 2D).

Top correlated genes with the principal components are insightful of disc homeostasis

To extract the most informative features of the PCA, we performed proteome-wide associations with each of the top three PCs, which accounted for over 70% of total variance, and presented the

bioRxiv preprint doi: https://doi.org/10.1101/2020.07.11.192948; this version posted November 21, 2020. The copyright holder for this preprint (which was not certified by peer review) is the author/funder. All rights reserved. No reuse allowed without permission.

top 100 most positively and top 100 most negatively correlated proteins for each of the PCs (Figure 2E-G). As expected, the correlation coefficients in absolute values were in the order of PC1 > PC2 > PC3 (Figure 2E-G). The protein content is presented as non-matrisome proteins (grey colour) and matrisome proteins (coloured) that are sub-categorised as previously. For the negatively correlated proteins, the matrisome proteins contributed to PC1 in distinguishing young disc samples, as well as to PC2 for sample location within the disc, but less so for disc level in PC3. Further, the relative composition of the core and non-core matrisome proteins varied between the three PCs, depicting the dynamic ECM requirement and its relevance in ageing (PC1), tissue composition within the disc (PC2) and mechanical loading (PC3).

PC1 of young discs identified known chondrocyte markers, CLEC3A (Lau et al., 2018) and LECT1/2 (Zhu et al., 2019); hedgehog signalling proteins, HHIPL2, HHIP, and SCUBE1 (Johnson et al., 2012); and xylosyltransferase-1 (XYLT1), a key enzyme for initiating the attachment of glycosaminoglycan side chains to proteoglycan core proteins (Silagi et al., 2018) (Figure 2E). Most of the proteins that were positively correlated in PC1 were coagulation factors or coagulation related, suggesting enhanced blood infiltration in aged discs. PC2 implicated key changes in molecular signalling proteins (hedgehog, WNT and Nodal) in the differences between the inner and outer disc regions (Figure 2F). Notably, PC2 contains heat shock proteins (HSPA1B, HSPA8, HSP90AA1, HSPB1) which are more strongly expressed in the OAF than in inner disc, indicating the OAF is under stress (Takao and Iwaki, 2002). Although the correlations in PC3 were much weaker, proteins such as CILP/CILP2, DCN, and LUM were associated with lower disc level.

ANOVA reveals the principal phenotypes for categories of ECMs

To investigate how age, disc compartment, level, and direction affect the protein profiles, we carried out ANOVA for each of these phenotypic factors for the categories of matrisome and non-matrisome proteins (Supplemental Figure S5H-J). In the young discs, the dominant phenotype explaining the variances for all protein categories was disc compartment. It is crucial that each disc compartment (NP, IAF and OAF) has the appropriate protein composition to function correctly (Supplemental Figure S5I). This also fits the understanding that young healthy discs are axially symmetric and do not vary across disc levels. In aged discs, compartment is still relevant for non-matrisome proteins and collagen, but disc level and directions become influential for other

bioRxiv preprint doi: https://doi.org/10.1101/2020.07.11.192948; this version posted November 21, 2020. The copyright holder for this preprint (which was not certified by peer review) is the author/funder. All rights reserved. No reuse allowed without permission.

protein categories, which is consistent with variations in mechanical loading occurring in the discs with ageing and degeneration (Supplemental Figure S5J). In the combined (young and aged) disc samples, age was the dominant phenotype across major matrisome categories, while compartment best explained the variance in non-matrisome, reflecting the expected changes in cellular (non-matrisome) and structural (matrisome) functions of the discs (Supplemental Figure S5H). This guided us to analyse the young and aged profiles separately, before performing cross-age comparisons.

The high-resolution spatial proteome of young and healthy discs

PCA of the 33 young profiles showed a distinctive separation of the OAF from the inner disc regions on PC1 (upper panel of Figure 3A). In PC2, the lower level L5/S1 could generally be distinguished from the upper lumbar levels (lower panel of Figure 3A). The detected proteome of the young discs (Figure 3B) accounts for 9.2% of the human proteome (or 1,883 out of the 20,368 on UniProt). We performed multiple levels of pairwise comparisons (summarised in Supplemental Figure S6A) to detect proteins associated with individual phenotypes, using three approaches (see Methods): statistical tests; proteins detected in one group only; or proteins using a fold-change threshold. We detected a set of 671 DEPs (Supplemental Table S2) (termed the 'variable set'), containing both matrisome and non-matrisome proteins (Figure 3D), and visualised in a heatmap (Supplemental Figure S7), with identification of four modules (Y1-Y4).

Expression modules show lateral and anteroposterior trends

To investigate how the modules are associated with disc components, we compared their protein expression profiles along the lateral and anteroposterior axes. The original $\log_2$(LFQ) values were transformed to z-scores to be on the same scale. Proteins of the respective modules were superimposed on the same charts, disc levels combined or separated (Figure 3E-H; Supplemental Figure S8). Module Y1 is functionally relevant to NP, containing previously reported NP and novel markers KRT19, CD109, KRT8 and CHRD (Anderson et al., 2002), CHRDL2, SCUBE1 (Johnson et al., 2012) and CLEC3B. Proteins levels in Y1 are lower on one side of the OAF, increases towards the central NP, before declining towards the opposing side, forming a concave pattern in both lateral and anteroposterior directions, with a shoulder drop occurring between IAF and OAF (Figure 3E).

bioRxiv preprint doi: https://doi.org/10.1101/2020.07.11.192948; this version posted November 21, 2020. The copyright holder for this preprint (which was not certified by peer review) is the author/funder. All rights reserved. No reuse allowed without permission.

Module Y2 was enriched in proteins for ECM organisation (FDR $q=8.8\times10^{-24}$); Y3 was enriched for proteins involved in smooth muscle contraction processes (FDR $q=8.96\times10^{-19}$); and Y4 was enriched for proteins of the innate immune system (FDR $q=2.93\times10^{-20}$). Interestingly, these modules all showed a tendency for convex patterns with upward expression toward the OAF regions, in both lateral and anteroposterior directions, in all levels, combined or separated (Figure 3F-H; Supplemental S8B-D). The higher proportions of ECM, muscle contraction and immune system proteins in the OAF are consistent with the contractile function of the AF (Nakai et al., 2016), and with the NP being avascular and "immune-privileged" in a young homeostatic environment (Sun et al., 2020).

Inner disc regions are characterised with NP markers

The most distinctive pattern on the PCA is the separation of the OAF from the inner disc, with 99 proteins expressed higher in the OAF and 55 expressed higher in the inner disc (Figure 3I,J). Notably, OAF and inner disc contained different types of ECM proteins. The inner disc regions were enriched in collagens (COL3A1, COL5A1, COL5A2, and COL11A2), matrillin (MATN3), and proteins associated with ECM synthesis (PCOLCE) and matrix remodelling (MXRA5). We also identified in the inner disc previously reported NP markers (KRT19, KRT8) (Risbud et al., 2015), in addition to inhibitors of WNT (FRZB, DKK3) and BMP (CHRD, CHRDL2) signalling (Figure 3I,J). Of note, FRZB and CHRDL2 were recently shown to have potential protective characteristics in osteoarthritis (Ji et al., 2019). The TGFβ pathway appears to be suppressed in the inner disc where antagonist CD109 (Bizet et al., 2011; Li et al., 2016) is highly expressed, and the TGFβ activity indicator TGFBI is expressed higher in the OAF than in the inner disc.

The OAF signature is enriched with proteins characteristic of tendon and ligament

The OAF is enriched with various collagens (COL1A1, COL6A1/2/3, COL12A1 and COL14A1), basement membrane (BM) proteins (LAMA4, LAMB2 and LAMC1), small leucine-rich proteoglycans (SLRP) (BGN, DCN, FMOD, OGN, PRELP), and BM-anchoring protein (PRELP) (Figure 3I,J). Tendon-related markers such as thrombospondins (THBS1/2/4) (Subramanian and Schilling, 2014) and cartilage intermediate layer proteins (CILP/CILP2) are also expressed higher in the OAF. Tenomodulin (TNMD) was exclusively expressed in 9 of the 12 young OAF profiles, and not in any other compartments (Supplemental Table S2). This fits a current understanding of

bioRxiv preprint doi: https://doi.org/10.1101/2020.07.11.192948; this version posted November 21, 2020. The copyright holder for this preprint (which was not certified by peer review) is the author/funder. All rights reserved. No reuse allowed without permission.

the AF as a tendon/ligament-like structure (Nakamichi et al., 2018). In addition, the OAF was enriched in actin-myosin (Figure 3I), suggesting a role of contractile function in the OAF, and in heat shock proteins (HSPA1B, HSPA8, HSPB1, HSP90B1, HSP90AA1), suggesting a stress response to fluctuating mechanical loads.

Spatial proteome enables clear distinction between IAF and OAF

We sought to identify transitions in proteomic signatures between adjacent compartments. The NP and NP/IAF protein profiles were highly similar (Supplemental Figure 6B). Likewise, NP/IAF and IAF showed few DEPs, except COMP which was expressed higher in IAF (Supplemental Figure 6C). OAF and NP (Supplemental Figure 6R), and OAF and NP/IAF (Supplemental Figure 6O) showed overlapping DEPs, consistent with NP and NP/IAF having highly similar protein profiles, despite some differences in the anteroposterior direction (Supplemental Figure 6P & Q). The clearest boundary within the IVD, between IAF and OAF, was marked by a set of DEPs, of which COL5A1, SERPINA5, MXRA5 were enriched in the IAF, whereas LAMB2, THBS1, CTSD typified the OAF (Supplemental Figure 6D). These findings agreed with the modular patterns (Figure 3E-H).

The constant set represents the baseline proteome among structures within the young disc

Of the 1,880 proteins detected, 1204 proteins were not found to vary with respect to the phenotypic factors. The majority of these proteins were detected in few profiles (Figure 3B) and were not used in the comparisons. We set a cutoff for a detection in >1/2 of the profiles to prioritise a set of 245 proteins, hereby referred to as the 'constant set' (Figure 3C). Both the variable and the constant sets contained high proportions of ECM proteins (Figure 3D). Amongst the proteins in the constant set that were detected in all 33 young profiles were known protein markers defining a young NP or disc, including COL2A1, ACAN and A2M (Risbud et al., 2015). Other key proteins in the constant set included CHAD, HAPLN1, VCAN, HTRA1, CRTAC1, and CLU. Collectively, these proteins showed the common characteristics shared by compartments of young discs, and they, alongside the variable set, form the architectural landscape of the young disc.

bioRxiv preprint doi: https://doi.org/10.1101/2020.07.11.192948; this version posted November 21, 2020. The copyright holder for this preprint (which was not certified by peer review) is the author/funder. All rights reserved. No reuse allowed without permission.

Diverse changes in the spatial proteome with ageing

Fewer inner-outer differences but greater variation between levels in aged discs

PCA was used to identify compartmental, directional and level patterns for the aged discs (Figure 4A). Albeit less clear than for the young discs (Figure 3A), the OAF could be distinguished from the inner disc regions on PC1, explaining 46.7% of the total variance (Figure 4A). PC2 showed a more distinct separation of signatures from lumbar disc levels L5/S1 to the upper disc levels (L4/L5 and L3/4), accounting for 21.8% of the total variance (Figure 4A).

Loss of the NP signature from inner disc regions

As with the young discs, we performed a series of comparative analyses (Figure 4C; Supplemental Figure S9 A-H; Supplemental Table S3). Detection of DEPs between the OAF and the inner disc (Figure 4B), showed that 100 proteins were expressed higher in the OAF, similar to young discs (Figure 3C). However, in the inner regions, only 9 proteins were significantly expressed higher, in marked contrast to the situation in young discs. Fifty-five of the 100 DEPs in the OAF region overlapped in the same region in the young discs, but only 3 of the 9 DEPs in the inner region were identified in the young disc; indicating changes in both regions but more dramatic in the inner region. This suggests that ageing and associated changes may have initiated at the centre of the disc. The typical NP markers (KRT8/19, CD109, CHRD, CHRDL2) were not detectable as DEPs in the aged disc; but CHI3L2, A2M and SERPING1 (Figure 4B), which have known roles in tissue fibrosis and wound healing (Lee et al., 2011; Naveau et al., 1994; Wang et al., 2019a), were detected uniquely in the aged discs.

Gradual modification of ECM composition and cellular responses in the outer AF

A comparative analysis of the protein profiles indicated that the aged OAF retained 55% of the proteins of a young OAF. These changes are primarily reflected in the class of SLRPs (BGN, DCN, FMOD, OGN, and PRELP), and glycoproteins such as CILP, CILP2, COMP, FGA/B, and FGG. From a cellular perspective, 45 proteins enriched in the aged OAF could be classified under 'responses to stress' (FDR $q=1.86\times10^{-7}$; contributed by CAT, PRDX6, HSP90AB1, EEF1A1, TUBB4B, P4HB, PRDX1, HSPA5, CRYAB, HIST1H1C), suggesting OAF cells are responding to a changing environment such as mechanical loading and other stress factors.

bioRxiv preprint doi: https://doi.org/10.1101/2020.07.11.192948; this version posted November 21, 2020. The copyright holder for this preprint (which was not certified by peer review) is the author/funder. All rights reserved. No reuse allowed without permission.

Convergence of the inner disc and outer regions in aged discs

To map the relative changes between inner and outer regions of the aged discs, we performed a systematic comparison between compartments (Supplemental Figure S9 A-D). The most significant observation was a weakening of the distinction between IAF and OAF that was seen in young discs, with only 17 DEPs expressed higher in the OAF of the aged disc (Supplemental Figure S9C). More differences were seen when we included the NP in the comparison with OAF (Supplemental Figure S9D), indicating some differences remain between inner and outer regions of the aged discs. While the protein profiles of the NP and IAF were similar, with no detectable DEPs (Supplemental Figure S9A & B), their compositions shared more resemblance with the OAF. These progressive changes of the protein profiles and DEPs between inner and outer compartments suggest the protein composition of the inner disc compartments becomes more similar to the OAF with ageing, with the greatest changes in the inner regions. This further supports a change initiating from the inner region of the discs with ageing.

Changes in young module patterns reflect convergence of disc compartments

We investigated protein composition in the young disc modules (Y1-Y4) across the lateral and anteroposterior axes (Figure 4C-F). For module Y1 that consists of proteins defining the NP region, the distinctive concave pattern has flattened along both axes, but more so for the anteroposterior direction where the clear interface between IAF and OAF was lost (Figure 4C; Supplemental Figure S9I). Similarly for modules Y2 and Y3, which consist of proteins defining the AF region, the trends between inner and outer regions of the disc have changed such that the patterns become more convex, with a change that is a continuum from inner to outer regions (Figure 4D,E; Supplemental Figure S9J,K). These changes in modules Y1-3 in the aged disc further illustrate the convergence of the inner and outer regions, with the NP/IAF becoming more OAF-like. For Y4, the patterns along the lateral and anteroposterior axes were completely disrupted (Figure 4F; Supplemental Figure S9J). As Y4 contains proteins involved in vascularity and inflammatory processes (Supplemental Table 5), these changes indicate disruption of cellular homeostasis in the NP.

bioRxiv preprint doi: https://doi.org/10.1101/2020.07.11.192948; this version posted November 21, 2020. The copyright holder for this preprint (which was not certified by peer review) is the author/funder. All rights reserved. No reuse allowed without permission.

Disc level variations reflect spatial and temporal progression of disc changes

The protein profiles of the aged disc levels, consistent with the PCA findings, showed similarity between L3/4 and L4/5 (Supplemental Figure S9E), but, in contrast to young discs, differences between L5/S1 and L4/5 (Supplemental Figure S9F), and more marked differences between L5/S1 and L3/4 (Supplemental Figure S9G,H). Overall, the findings from PCA, protein profiles (Figure 2B-D) and MRI (Figure 1C) agree. As compared to young discs, the more divergent differences across the aged disc levels potentially reflect progressive transmission from the initiating disc to the adjacent discs with ageing. To further investigate the aetiologies underlying IDD, cross-age comparisons are needed.

Aetiological insights uncovered by young/aged comparisons

Next, we performed extensive pair-wise comparisons between the young and aged samples under a defined scheme (Supplemental Figure S10A; Supplemental Table S4). First, we compared all 33 young samples with all 33 aged samples, which identified 169 DEPs with 104 expressed higher in the young and 65 expressed higher in the aged discs (Figure 5A). A simple GO term analysis showed that the most important biological property for a young disc is structural integrity, which is lost in aged discs (Figure 5B; Supplemental Table S5). The protein classes most enriched in the young discs were related to cartilage synthesis, chondrocyte development, and ECM organisation (Figure 5B). The major changes in the aged discs relative to young ones, were proteins involved in cellular responses to an ageing environment, including inflammatory and cellular stress signals, progressive remodelling of disc compartments, and diminishing metabolic activities (Figure 5C; Supplemental Table S5).

Inner disc regions present with most changes in ageing

For young versus old discs, we compared DEPs of the whole disc (Figure 5A) with those from the inner regions (Figure 5D) and OAF (Figure 5E) only. Seventy-five percent (78/104) of the down-regulated DEPs (Figure 5F) were attributed to the inner regions, and only 17% (18/104) were attributed to the OAF (Figure 5F). Similarly, 65% (42/65) of the up-regulated DEPs were solely contributed by inner disc regions, and only 18.4% (12/65) by the OAF. Only 5 DEPs were higher

bioRxiv preprint doi: https://doi.org/10.1101/2020.07.11.192948; this version posted November 21, 2020. The copyright holder for this preprint (which was not certified by peer review) is the author/funder. All rights reserved. No reuse allowed without permission.

in the OAF, while 49 were uniquely up-regulated in the inner discs (Figure 5G). The key biological processes in each of the compartments are highlighted in Figure 5F & G.

The changing biological processes in the aged discs

Expression of known NP markers was reduced in aged discs, especially proteins involved in the ECM and its remodelling, where many of the core matrisome proteins essential for the structural function of the NP were less abundant or absent. While this is consistent with previous observations (Feng et al., 2006), of interest was the presence of a set of protein changes that were also seen in the OAF, which was also rich in ECM and matrix remodelling proteins (HTRA1, SERPINA1, SERPINA3, SERPINC1, SERPINF1, and TIMP3) and proteins involved in fibrotic events (FN1, POSTN, APOA1, APOB), suggesting these changes are occurring in the aging IVDs (Figure 5 F,G).

Proteins associated with cellular stress are decreased in the aged inner disc, with functions ranging from molecular chaperones needed for protein folding (HSPB1, HSPA1B and HSPA9) to modulation of oxidative stress (SOD1) (Figure 5F). SOD1 has been shown to become less abundant in the aged IVD (Hou et al., 2014) and in osteoarthritis (Scott et al., 2010). HSPB1 is cytoprotective and a deficiency is associated with inflammation reported in degenerative discs (Wuertz et al., 2012). We found an increased concentration of clusterin (CLU) (Figure 5G), an extracellular chaperone that aids the solubilisation of misfolded protein complexes by binding directly and preventing protein aggregation (Trougakos, 2013; Wyatt et al., 2009), and also has a role in suppressing fibrosis (Peix et al., 2018).

Inhibitors of WNT (DKK3 and FRZB), and antagonists of BMP/TGFβ (CD109, CHRDL2, DCN FMOD, INHBA and THBS1) signalling were decreased or absent in the aged inner region (Figure 5F,G), consistent with the reported up-regulation of these pathways in IDD (Hiyama et al., 2010) and its closely related condition osteoarthritis (Leijten et al., 2013). Targets of hedgehog signalling (HHIPL2 and SCUBE1) were also reduced (Figure 5F), consistent with SHH's key roles in IVD development and maintenance (Rajesh and Dahia, 2018). TGFβ signalling is a well-known pathway associated with fibrotic outcomes. WNT is known to induce chondrocyte hypertrophy (Dong et al., 2006), that can be enhanced by a reduction in S100A1 (Figure 5F), a known inhibitor of chondrocyte hypertrophy (Saito et al., 2007).

bioRxiv preprint doi: https://doi.org/10.1101/2020.07.11.192948; this version posted November 21, 2020. The copyright holder for this preprint (which was not certified by peer review) is the author/funder. All rights reserved. No reuse allowed without permission.

To gain an overview of the disc compartment variations between young and aged discs, we followed the same strategy as in Supplemental Figure S7 to aggregate three categories of DEPs in all 23 comparisons (Supplemental Figure S10A) and created a heatmap from the resulting 719 DEPs. This allowed us to identify 6 major protein modules (Figure 5H). A striking feature is module 6 (M6), which is enriched for proteins involved in the complement pathway (GSEA Hallmark FDR $q=4.9\times10^{-14}$) and angiogenesis ($q=2.3\times10^{-3}$). This module contains proteins that are all highly expressed in the inner regions of the aged disc, suggesting the presence of blood. M6 also contains the macrophage marker CD14, which supports this notion.

We visualised the relationship between the young (Y1-4) and young/aged (M1-6) modules using an alluvial chart (Figure 5I). Y1 corresponds primarily to M1b that is enriched with fibrosis, angiogenesis, apoptosis and EMT (epithelial to mesenchymal transition) proteins. Y2 seems to have been deconstructed into three M modules (M2b > M3 > M4). M2b and M3 contain proteins linked to heterogeneous functions, while proteins in M4 are associated with myogenesis and cellular metabolism, but also linked to fibrosis and angiogenesis. Y3 primarily links to M2a with a strong link to myogenesis, and mildly connects with M3 and M4. Y4 has the strongest connection with M6a, which is linked to coagulation. Both the variable and the constant sets of the young disc were also changed in ageing. In the constant set, there is a higher tendency for a decrease in ECM-related proteins, and an increase in blood and immune related proteins with ageing, that may reflect an erosion of the foundational proteome, and infiltration of immune cells (Figure S10L).

In all, the IVD proteome showed that with ageing, activities of the SHH pathways were decreased, while those of the WNT and BMP/TGFβ pathways, EMT, angiogenesis, fibrosis, cellular stresses and chondrocyte hypertrophy-like events were increased.

Concordant changes between the transcriptome and proteome of disc cells

The proteome reflects both current and past transcriptional activities. To investigate upstream cellular and regulatory activities, we obtained transcriptome profiles from two IVD compartments (NP and AF) and two sample states (young, scoliotic but non-degenerated, YND; aged individuals with clinically diagnosed IDD, AGD) (Table 1). The transcriptome profiles of YND and AGD are similar to the young and aged disc proteome samples, respectively. After normalisation (Supplemental Figure S11A) and hierarchical clustering, we found patterns reflecting relationships

bioRxiv preprint doi: https://doi.org/10.1101/2020.07.11.192948; this version posted November 21, 2020. The copyright holder for this preprint (which was not certified by peer review) is the author/funder. All rights reserved. No reuse allowed without permission.

among IVD compartments and ages/states (Supplemental Figure S11B-D). PCA of the transcriptome profiles showed that PC1 captured age/state variations (Figure 6A) and PC2 captured the compartment (AF or NP) differences, with a high degree of similarity to the proteomic PCA that explained 65.0% of all data variance (Figure 2A).

Transcriptome shows AF-like characteristics of the aged/degenerated NP

We compared the transcriptome profiles of different compartments and age/state-groups (Supplemental Figure S11E-H). We detected 88 DEGs (differentially expressed genes; Methods) between young AF and young NP samples (Supplemental Figure S11E); 39 were more abundant in young NP (including known NP markers *CD24*, *KRT19*) and 49 were more abundant in young AF, including the AF markers, *COL1A1* and *THBS1*. In the AGD samples, 11 genes differed between AF and NP (Supplemental Figure S11F), comparable to the proteome profiles (Figure 4C). Between the YND and AGD AF, there were 45 DEGs, with *COL1A1* and *MMP1* more abundant in YND and *COL10A1*, WNT signalling (*WIF1*, *WNT16*), inflammatory (*TNFAIP6*, *CXCL14*, *IL11*), and fibrosis-associated (*FN1*, *CXCL14*) genes more abundant in AGD (Supplemental Figure S11G). The greatest difference was between YND and AGD NP, with 216 DEGs (Supplemental Figure S11H), with a marked loss of NP markers (*KRT19*, *CD24*), and gain of AF (*THBS1*, *DCN*), proteolytic (*ADAMTS5*), and EMT (*COL1A1*, *COL3A1*, *PDPN*, *NT5E*, *LTBP1*) markers with age. Again, consistent with the proteomic findings, the most marked changes are in the NP, with the transcriptome profiles becoming AF-like.

Concordance between transcriptome and proteome profiles

We partitioned the DEGs between the YND and AGD into DEGs for individual compartments (Figure 6B). The transcriptomic (Figure 6B) Venn diagram was very similar to the proteomic one (Figure 5F-G). For example, WNT/TGFβ antagonists and ECM genes were all down-regulated with ageing/degeneration, while genes associated with stress and ECM remodelling were more common. When we directly compared the transcriptomic DEGs and proteomic DEPs across age/states and compartments (Figure 6C-F), we observed strong concordance between the two types of datasets for a series of markers. In the young discs, concordant markers included *KRT19* and *KRT8*, *CHRDL2*, *FRZB*, and *DKK3* in the NP, and *COL1A1*, *SERPINF1*, *COL14A1*, and *THBS4* in the AF (Figure 6C). In the AGD discs, concordant markers included *CHI3L2*, *A2M* and

bioRxiv preprint doi: https://doi.org/10.1101/2020.07.11.192948; this version posted November 21, 2020. The copyright holder for this preprint (which was not certified by peer review) is the author/funder. All rights reserved. No reuse allowed without permission.

ANGPTL4 in the NP and *MYH9*, *HSP90AB1*, *HBA1*, and *ACTA2* in the AF (Figure 6D). A high degree of concordance was also observed when we compared across age/states for the AF (Figure 6E) and NP (Figure 6F).

Despite the transcriptomic samples having diagnoses (scoliosis for YND and IDD for AGD), whereas the proteome samples were cadaver samples with no reported diagnosis of IDD, the changes detected in the transcriptome profiles substantially support the proteomic findings. A surprising indication from the transcriptome was the increased levels of *COL10A1* (Lu et al., 2014), *BMP2* (Grimsrud et al., 2001), *IBSP*, defensin beta-1 (*DEFB1*), *ADAMTS5*, pro-inflammatory (*TNFAIP6*, *CXCL*) and proliferation (*CCND1*, *IGFBP*) genes in the AGD NP (Supplemental Figure S11E-H), reaffirming the involvement of hypertrophic-like events (Melas et al., 2014) in the aged and degenerated NP.

The genome-wide transcriptomic data included over 20 times more genes per profile than the proteomic data, providing additional biological information about the disc, particularly low abundance proteins, such as transcription factors and surface markers. For example, additional WNT antagonists were *WIF1* (Wnt inhibitory factor) and *GREM1* (Figure 6B) (Leijten et al., 2013). Comparing the YND NP against YND AF or AGD NP (Supplemental Figure S11E,H), we identified higher expression of three transcription factors, *T* (brachyury), *HOPX* (homeodomain-only protein homeobox), and *ZNF385B* in the YND NP. Brachyury is a well-known marker for the NP (Risbud et al., 2015), and *HOPX* is differentially expressed in mouse NP as compared to AF (Veras et al., 2020), and expressed in mouse notochordal NP cells (Lam, 2013). Overall, transcriptomic data confirmed the proteomic findings and revealed additional markers.

Changes in the active proteome in the ageing IVD

The proteomic data up to this point is a static form of measurement (static proteome) and represents the accumulation and turnover of all proteins up to the time of harvest. The transcriptome indicates genes that are actively transcribed, but does not necessarily correlate to translation or protein turnover. Thus, we studied changes in the IVD proteome (dynamic proteome) that would reflect newly synthesised proteins and proteins cleaved by proteases (degradome), and how they relate to the static proteomic and transcriptomic findings reported above.

bioRxiv preprint doi: https://doi.org/10.1101/2020.07.11.192948; this version posted November 21, 2020. The copyright holder for this preprint (which was not certified by peer review) is the author/funder. All rights reserved. No reuse allowed without permission.

Aged or degenerated discs synthesise fewer proteins

We performed e*x vivo* labelling of newly synthesised proteins using the SILAC protocol (Ong et al., 2002) (Figure 7A; Methods) on AF and NP samples from 4 YND individuals and one AGD individual (Table 1). In the SILAC profiles, light isotope-containing signals correspond to the pre-existing unlabelled proteome, and heavy isotope-containing signals to newly synthesised proteins (Figure 7B). The ECM compositions in the light isotope-containing profiles (Figure 7B, middle panel) are similar to the static proteome samples of the corresponding age groups described above (Figure 1F). Although for NP_YND152, the numbers of identified proteins in the heavy profiles are considerably less than NP_YND151 due to a technical issue during sample preparation, it is overall still more similar to NP_YND152 than to other samples (Supplemental Figure S12B), indicating that its biological information is still representative of a young NP and the respective AF samples are similar. In contrast, the heavy isotope-containing profiles contained fewer proteins in the AGD than in the YND samples (Figure 7B, left panel) and showed variable heavy to light ratio profiles (Figure 7B, right panel).

To facilitate comparisons, we averaged the abundance of the proteins detected in the NP or AF for which we had more than one sample, then ranked the abundance of the heavy isotope-containing (Figure 7C) and light isotope-containing (Figure 7D) proteins. The number of proteins newly synthesised in the AGD samples was about half that in the YND samples (Figure 7C). This is unlikely to be a technical artefact as the total number of light isotope-containing proteins detected in the AGD samples is comparable to the YND, in both AF and NP (Figure 7D), and the difference is again well illustrated in the heavy to light ratios (Figure 7E).

Reduced synthesis of non-matrisome proteins was found for the AGD samples (GAPDH as a reference point (dotted red lines) (Figures 7C & D; Figure 7C & E, grey portions). Of the 68 high abundant non-matrisome proteins in the YND NP compartment that were not present in the AGD NP, 28 are ribosomal proteins (Supplemental Figure S12C), suggesting reduced translational activities. This agrees with our earlier findings of cellularity, as represented by histones, in the static proteome (Figure 1J, K).

Changes in protein synthesis in response to the cell microenvironment affects the architecture of the disc proteome. To understand how the cells may contribute and respond to the accumulated

bioRxiv preprint doi: https://doi.org/10.1101/2020.07.11.192948; this version posted November 21, 2020. The copyright holder for this preprint (which was not certified by peer review) is the author/funder. All rights reserved. No reuse allowed without permission.

matrisome in the young and aged disc, we compared the newly synthesised matrisome proteins of AGD and YND samples rearranged in order of abundance (Figure 7E). More matrisome proteins were synthesised in YND samples across all classes. In YND AF, collagens were synthesised in higher proportions than in AGD AF with the exception of fibril-associated COL12A1 (Figure 7E, top panel). Similarly, higher proportions in YND AF were observed for proteoglycans (except FMOD), glycoproteins (except TNC, FBN1, FGG and FGA), ECM affiliated proteins (except C1QB), ECM regulators (except SERPINF2, SERPIND1, A2M, ITIH2, PLG), and secreted factors (except ANGPTL2). Notably, regulators that were exclusively synthesised in young AF are involved in collagen synthesis (P4HA1/2, LOXL2, LOX, PLOD1/2) and matrix turnover (MMP3), with enrichment of protease HTRA1 and protease inhibitors TIMP3 and ITIH in YND AF compared to AGD AF.

In AGD NP, overall collagen synthesis was less than in YND NP (Figure 7E, lower panel); however, there was more synthesis of COL6A1/2/3 and COL12A1. Furthermore, AGD NP synthesised more LUM, FMOD, DCN, PRG4, and PRELP proteoglycans than YND NP. Notably, there was less synthesis of ECM-affiliated proteins (except C1QC and SEMA3A) and regulators – particularly those involved in collagen synthesis (P4HA1/2, LOXL2, LOX) – but an increase in protease inhibitors. A number of newly synthesised proteins in AGD NP were similarly represented in the transcriptome data, including POSTN, ITIH2, SERPINC1, IGFBP3, and PLG. Some genes were simultaneously underrepresented in the AGD NP transcriptome and newly synthesised proteins, including hypertrophy inhibitor GREM1 (Leijten et al., 2013).

Proteome of aged or degenerated discs is at a higher degradative state

The degradome reflects protein turnover by identifying cleaved proteins in a sample (Lopez-Otin and Overall, 2002). When combined with relative quantification of proteins through the use of isotopic and isobaric tagging and enrichment for cleaved neo amine (N)-termini of proteins before labelled samples are quantified by mass-spectrometry, degradomics is a powerful approach to identify the actual status of protein cleavage *in vivo.*

We employed the well-validated and sensitive terminal amine isotopic labelling of substrates (TAILS) method (Kleifeld et al., 2010; Rauniyar and Yates, 2014) to analyse and compare 6 discs from 6 individuals (2 young and non-degenerated, YND; and 4 aged and/or degenerated, AGD)

bioRxiv preprint doi: https://doi.org/10.1101/2020.07.11.192948; this version posted November 21, 2020. The copyright holder for this preprint (which was not certified by peer review) is the author/funder. All rights reserved. No reuse allowed without permission.

(Table 1) (Figure 7F) (Kleifeld et al., 2010; Rauniyar and Yates, 2014) using the 6-plex tandem mass tag (TMT)-TAILS (labelling 6 independent samples and analysed together on the mass spectrometer) (Figure 7F). Whereas shotgun proteomics is intended to identify the proteome components, N-terminome data is designed to identify the exact cleavage site in proteins that also evidence stable cleavage products *in vivo*.

Here, TAILS identified 123 and 84 cleaved proteins in the AF and NP disc samples, respectively. Performing hierarchical clustering on the data we found that the two YND samples (136 and 141; Table 1) tend to cluster together in both AF and NP (Figure 7G,H; Supplemental Figure S13A,B). Interestingly, the trauma sample AGD143 (53yr male), who has no known IDD diagnosis, tend to cluster with other clinically diagnosed AGD samples, in both AF and NP. This might be because AGD143 has unreported degeneration or ageing is a dominant factor in degradome signals.

We identified two protein/peptide modules in the AF (Figure 7G), corresponding to more degradation/cleaving in YND AF (magenta) and AGD AF (blue), respectively. There are only 13 unique proteins for proteins/peptides more degraded in the YND AF, the most common of which is COL1A1/2, followed by COL2A1. In comparison, the module corresponding to more degradation in AGD AF recorded 24 unique proteins, 7 (CILP, CILP2, COL1A1, COMP, HBA1, HBB, PRELP) of which are in strong overlap (χ^2 $p=2.0\times10^{-71}$) with the 99 proteins higher in outer AF in the spatial proteome (Figure 3I). This indicates that key proteins defining a young outer AF is experiencing faster degradation in aged and degenerated samples.

Similarly, we identified two modules in the NP (Figure 7H), whereby one (magenta) corresponds to more degradation in the YND, and the other (blue) corresponds to more degradation in the AGD. Only 10 unique proteins were recorded in the magenta module (for YND), with COL2A1 being the most dominant 928 peptides); whereas 32 were recorded for the blue module (for AGD). Overall, there are more unique proteins involved in faster degradation in AGD AF and NP.

MRI landscape correlates with proteomic landscape

We tested for a correlation between MRI signal intensity and proteome composition. In conventional 3T MRI of young discs, the NP is brightest reflecting its high hydration state while the AF is darker, thus less hydrated (Figure 1B; Supplemental Figure S14B). Since aged discs

bioRxiv preprint doi: https://doi.org/10.1101/2020.07.11.192948; this version posted November 21, 2020. The copyright holder for this preprint (which was not certified by peer review) is the author/funder. All rights reserved. No reuse allowed without permission.

present with more MRI phenotypes, we used higher resolution MRI (7T) on them (Figure 1C; Figure 8A), which showed less contrast between NP and AF than in the young discs. To enhance robustness, we obtained three transverse stacks per disc level for the aged discs (Figure 8B; Supplemental Figure S14D), and averaged the pixel intensities for the different compartments showing that overall, the inner regions were still brighter than the outer (Figure 8C).

Next, we performed a level-compartment bi-clustering on the pixel intensities of the aged disc MRIs, which was bound by disc level and compartment (Figure 8D). The findings resembled the proteomic clustering and PCA patterns (Figure 2; Supplemental Figure S6V-W). We performed a pixel intensity averaging of the disc compartments from the 3T images (Supplemental Figure 13B), and a level-compartment bi-clustering on the pixel intensities (Supplemental Figure S14C). While the clustering can clearly partition the inner from the outer disc compartments, the information value from each of the compartments is less due to the lower resolution of the MRI. In all, these results indicate a link between regional MRI landscapes and proteome profiles, prompting us to investigate their potential connections.

Proteome-wide associations with MRI landscapes reveals a hydration matrisome

The MRI and the static proteome were done on the same specimens in both individuals, so we could perform proteome-wide associations with the MRI intensities. We detected 85 significantly correlated ECM proteins, hereby referred to as the hydration matrisome (Figure 8E). We found no collagen to be positively correlated with brighter MRI, which fits current understanding as collagens contribute to fibrosis and dehydration. Other classes of matrisome proteins were either positively or negatively correlated, with differential components for each class (Figure 8E). Positively correlated proteoglycans included EPYC, PRG4 (lubricin) and VCAN, consistent with their normal expression in a young disc and hydration properties. Negatively correlated proteins included OAF (TNC, SLRPs) and fibrotic (POSTN) markers (Figure 8E).

Given this MRI-proteome link and the greater dynamic ranges of MRI in the aged discs enabled by the higher resolution 7T MRIs (Figure 8D), we hypothesised that the hydration matrisome might be used to provide information about MRI intensities and thus disc hydration. To test this, we trained a LASSO regression model (Tibshirani, 1996) of the aged MRIs using the hydration matrisome (85 proteins), and applied the model to predict the intensity of the MRIs of the young

bioRxiv preprint doi: https://doi.org/10.1101/2020.07.11.192948; this version posted November 21, 2020. The copyright holder for this preprint (which was not certified by peer review) is the author/funder. All rights reserved. No reuse allowed without permission.

discs, based on the young proteome of the same 85 proteins. Remarkably, we obtained a PCC of 0.689 ($p=8.9\times10^{-6}$; Spearman=0.776) between the actual and predicted MRI (Supplemental Figure S14E). The predicted MRI intensities of the young disc exhibited a smooth monotonic decrease from the NP towards IAF, then dropped suddenly towards the OAF (Figure 8F, right panel), with an ROC AUC (receiver operating characteristics, area under the curve) of 0.996 between IAF and OAF (Supplemental Figure S14F). In comparison, actual MRIs exhibited a linear decrease from NP to OAF (Figure 8F, left panel). On reviewing these two patterns, we argue that the predicted intensities may be a more faithful representation of the young discs' water contents than the actual MRI, as it reflects the gross images (Supplemental Figure S1A), PCA (Figure 3A) and Y1 modular trend in the young discs (Figure 3E). This exercise not only revealed the inherent connections between regional MRI and regional proteome, but also identified a set of ECM components that is predictive of MRI relating to disc hydration, which may be valuable for future clinical applications.

bioRxiv preprint doi: https://doi.org/10.1101/2020.07.11.192948; this version posted November 21, 2020. The copyright holder for this preprint (which was not certified by peer review) is the author/funder. All rights reserved. No reuse allowed without permission.

Discussion

Here, we present DIPPER – a human IVD proteomic resource comprising point-reference genome-wide profiles. The discovery dataset was established from intact lumbar discs of a young cadaver with no history of skeletal abnormalities (e.g. scoliosis), and an aged cadaver with reduced IVD MRI intensity and annular tears. Although these two individuals may not be representative of their respective age-groups, this is the first known attempt to achieve high spatial resolution profiles in the discs, adding a critical and much needed dimension to the current available IVD proteomic datasets. We showed that our spatiotemporal proteomes integrate well with the dynamic proteome and transcriptome of clinical samples, demonstrating their application values with other datasets.

In creating the point-references, we use a well-established protein extraction protocol (Onnerfjord et al., 2012b), and chromatographic fractionation of the peptides prior to mass spectrometry, we produced a dataset of the human intervertebral disc comprising 3,100 proteins, encompassing ~400 matrisome and 2,700 non-matrisome proteins, with 1,769 proteins detected in 3 or more profiles, considerably higher than recent studies (Maseda et al., 2016; Rajasekaran et al., 2020; Ranjani et al., 2016; Sarath Babu et al., 2016). The high quality of our data enabled the application of unbiased approaches including PCA and ANOVA to reveal the relative importance of the phenotypic factors. Particularly, age was found to be the dominant factor influencing proteome profiles.

Comparisons between different compartments of the young disc produced a reference landscape containing known (KRT8/19 for the NP; COL1A1, CILP and COMP for the AF) and novel (FRZB, CHRD, CHRDL2 for the NP; TNMD, SLRPs and SOD1 for the AF) markers. The young healthy discs were enriched for matrisome components consistent with a healthy functional young IVD. Despite morphological differences between NP and IAF, the inner disc compartments (NP, NP/IAF and IAF) display high similarities, in contrast to the large differences between IAF and OAF, which was consistent for discs from all lumbar disc levels. This morphological-molecular discrepancy might be accounted for by subtle differences in the ECM organisation, such as differences in GAG moieties on proteoglycans, or levels of glycosylation or other modifications of ECM that diversify function (Silagi et al., 2018). Nonetheless, we partitioned the detected proteins into a variable set that captures the diversity, and a constant set that lays the common foundation of all young compartments, which work in synergy to achieve disc function.

bioRxiv preprint doi: https://doi.org/10.1101/2020.07.11.192948; this version posted November 21, 2020. The copyright holder for this preprint (which was not certified by peer review) is the author/funder. All rights reserved. No reuse allowed without permission.

Clustering analysis of the 671 DEPs of the variable set identified 4 key modules (Y1-Y4). Visually, Y1 and Y2 mapped across the lateral and anteroposterior axes with opposing trends. Molecularly, module Y1 (NP) contained proteins promoting regulation of matrix remodelling, such as matrix degradation inhibitor MATN3 (Jayasuriya et al., 2012) and MMP inhibitor TIMP1. Inhibitors of WNT and BMP signalling were also present. Module Y2 (OAF) included COL1A1, THBS1/2/3, CILP1/CILP2 and TNMD, consistent with the OAF's tendon-like features (Nakamichi et al., 2018). It also included a set of SLRPs that might play roles in regulation of collagen assembly (Robinson et al., 2017; Taye et al., 2020), fibril alignment (Robinson et al., 2017), maturation and crosslinking (Kalamajski et al., 2016); while others are known to inhibit or promote TGFβ signalling (Markmann et al., 2000). Notably, the composition of the IAF appeared to be a transition zone between NP and OAF rather than an independent compartment, as few proteins can distinguish it from adjacent compartments. Classes of proteins in both Y3 (smooth muscle feature) and Y4 (immune and blood) resemble Y2, which reflects the contractile property of the AF (Nakai et al., 2016) and the capillaries infiltrating or present at the superficial outer surface of the IVD.

In the aged disc, the change in the DEPs between the inner and outer regions of the discs suggests extensive changes in the inner compartment(s). Mapping the aged data onto modules Y1-Y4 allowed a visualisation of the changes. The flattening of the Y1 and Y2 modules along both the lateral and anteroposterior axes indicated a convergence of the inner and outer disc. This is supported by the observed rapid decline of NP proteins and increase of AF proteins in the inner region. Fewer changes were seen in the aged OAF, which concurs with the notion that degenerative changes originate from the NP and radiate outwards, however, infringement of IAF into the NP cannot be excluded. The most marked change was seen in module Y4 (blood), where the pattern was inverted, characterised by high expression in the NP but low in OAF. While contamination cannot be excluded and there are reports that capillaries do not infiltrate the NP even in degeneration (Nerlich et al., 2007), our finding is consistent with other proteomic studies showing enrichment of blood proteins in pathological NP (Maseda et al., 2016). The route of infiltration can be from the fissured AF or cartilage endplates. Calcified endplates are more susceptible to microfractures, which can lead to blood infiltration into the NP (Sun et al., 2020). Of interest is the involvement of an immune response within the inner disc. This corroborates reports of inflammatory processes in ageing and degenerative discs, with the up-regulation of pro-

bioRxiv preprint doi: https://doi.org/10.1101/2020.07.11.192948; this version posted November 21, 2020. The copyright holder for this preprint (which was not certified by peer review) is the author/funder. All rights reserved. No reuse allowed without permission.

inflammatory cytokines and presence of inflammatory cells (Molinos et al., 2015; Wuertz et al., 2012).

The SILAC and degradome studies provided important insights into age-related differences in the biosynthetic and turnover activity in the IVD. The SILAC data indicated that protein synthesis is significantly impaired in aged degenerated discs. These findings correlate with reports of reduced cellularity in ageing (Rodriguez et al., 2011), which we have also ascertained by leveraging the relationship of histones and housekeeping genes with cell numbers. From the TAILS degradome analysis, we observed more cleaved protein fragments in aged compartments, particularly for structural proteins important for tissue integrity such as COMP and those involved in cell-matrix interactions such as FN1, which was coupled with the enrichment of the proteolytic process GO terms in the aged static proteome. Collectively, this reveals a systematic modification and replacement of the primary proteomic architecture of the young IVD with age that is associated with diminished or failure in functional properties in ageing or degeneration.

Despite known transcriptome-proteome discordance (Fortelny et al., 2017), our identification of concordant changes allow insights into active changes in the young and aged discs. For example, inhibitors of the WNT pathway and antagonists of BMP/TGFβ signalling (Leijten et al., 2013) were down regulated in the aged discs in both the proteome and transcriptome. Interestingly, the activation of these pathways is known to promote chondrocyte hypertrophy (Dong et al., 2006), and hypertrophy has been noted in IDD (Rutges et al., 2010). This suggests a model where the regulatory environment suppressing cellular hypertrophy changes with ageing or degeneration, resulting in conditions such as cellular senescence and tissue mineralisation that are part of the pathological process. In support, S100A1, a known inhibitor of chondrocyte hypertrophy (Saito et al., 2007) is down regulated, while chondrocyte hypertrophy markers *COL10A1* and *IBSP* (Komori, 2010) are up-regulated in the aged disc. Similar changes have been observed in ageing mouse NP (Veras et al., 2020) as well as in osteoarthritis (Zhu et al., 2009) where chondrocyte hypertrophy is thought to be involved in its aetiology (Ji et al., 2019; van der Kraan and van den Berg, 2012). Given that WNT inhibitors are already in clinical trials for osteoarthritis (Wang et al., 2019b), this may point to a prospective therapeutic strategy for IDD.

bioRxiv preprint doi: https://doi.org/10.1101/2020.07.11.192948; this version posted November 21, 2020. The copyright holder for this preprint (which was not certified by peer review) is the author/funder. All rights reserved. No reuse allowed without permission.

A key finding of our study is the direct demonstration, within a single individual, of association between the hydration status of the disc as revealed by MRI, and the matrisome composition of the disc proteome. The remarkable correlation between predicted hydration states inferred from the spatial proteomic data and the high-definition phenotyping of the aged disc afforded by 7T MRI has enormous potential for understanding the molecular processes underlying IDD.

In conclusion, we have generated point-reference datasets of the young and aged disc proteome, at a significantly higher spatial resolution than previous works. By means of a methodological framework, we revealed compartmentalised information on the ECM composition and cellular activities, and their changes with ageing. Integration of this point-reference with additional age- and protein-specific information of synthesis/degradation help gain insights into the underlying molecular pathology of degeneration (Figure 8G & H). The richness of information in DIPPER makes it a valuable resource for cross referencing with human, animal and *in vitro* studies to evaluate clinical relevance and guide the development of therapeutics for human IDD.

bioRxiv preprint doi: https://doi.org/10.1101/2020.07.11.192948; this version posted November 21, 2020. The copyright holder for this preprint (which was not certified by peer review) is the author/funder. All rights reserved. No reuse allowed without permission.

Materials and methods

Cadaveric specimens

Two human lumbar spines were obtained through approved regulations and governing bodies, with one young (16M) provided by L.H. (McGill University) and one aged (59M) from Articular Engineering, LLC (IL, USA). The young lumbar spine was received frozen as an intact whole lumbar spine. The aged lumbar spine was received frozen, dissected into bone-disc-bone segments. The cadaveric samples were stored at -80^{0}C until use.

Clinical specimens

Clinical specimens were obtained with approval by the Institutional Review Board (references UW 13-576 and EC 1516-00 11/01/2001) and with informed consent in accordance with the Helsinki Declaration of 1975 (revision 1983) from another 15 patients undergoing surgery for IDD, trauma or adolescent idiopathic scoliosis at Queen Mary Hospital (Hong Kong), and Duchess of Kent Children's Hospital (Hong Kong). Information of both the cadaveric and clinical samples are summarised in Table 1.

MRI imaging of cadaveric samples

The discs were thawed overnight at 4^{0}C, and then pre-equalised for scanning at room temperature. For the young IVD, these were imaged together as the lumbar spine was kept intact. T2-weighted and T1-weighted sagittal and axial MRI, T1-rho MRI and Ultrashort-time-to-echo MRI images were obtained using a 3T Philips Achieva 3.0 system at the Department of Diagnostic Radiology, The University of Hong Kong.

For the aged discs, the IVD were imaged separately as bone-disc-bone segments, at the Department of Electrical and Electronic Engineering, The University of Hong Kong. The MRS and CEST imaging were performed. The FOV for the CEST imaging was adjusted to 76.8×76.8 mm^2 to accommodate the size of human lumbar discs (matrix size = 64×64, slice thickness = 2 mm). All MRI experiments were performed at room temperature using a 7 T pre-clinical scanner (70/16 Pharmascan, Bruker BioSpin GmbH, Germany) equipped with a 370 mT/m gradient system along

bioRxiv preprint doi: https://doi.org/10.1101/2020.07.11.192948; this version posted November 21, 2020. The copyright holder for this preprint (which was not certified by peer review) is the author/funder. All rights reserved. No reuse allowed without permission.

each axis. Single-channel volume RF coils with different diameters were used for the samples based on size (60 mm for GAG phantoms and human cadaveric discs).

Image assessment of the aged lumbar IVD

The MRI images in the transverse view were then assessed for intensity of the image (brighter signifying more water content). Three transverse MRI images per IVD were overlaid with a grid representing the areas that were cut for mass-spectrometry measurements as outlined previously. For each region, the 'intensity' was represented by the average of the pixel intensities, which were graphically visualised and used for correlative studies.

Division of cadaveric IVD for mass spectrometry analysis

The endplates were carefully cut off with a scalpel, exposing the surface of the IVD, which were then cut into small segments spanning seven segments in the central left-right lateral axis, and five segments in the central anteroposterior axis (Figure 1C). In all, this corresponds to a total of 11 locations per IVD. Among them, 4 are from the OAF, 2 from the IAF (but only in the lateral axis), 1 from the central NP, and 4 from a transition zone between IAF and the NP (designated the 'NP/IAF'). Samples were stored frozen at -80^{0}C until use.

SILAC by ex vivo culture of disc tissues

NP and AF disc tissues from spine surgeries (Table 1) were cultured in custom-made Arg- and Lys-free α-MEM (AthenaES) as per formulation of Gibco α-MEM (Cat #11900-024), supplemented with 10% dialysed FBS (10,000 MWCO, Biowest, Cat# S181D), penicillin/streptomycin, 2.2 g/L sodium bicarbonate (Sigma), 30 mg/L L-methionine (Sigma), 21 mg/L "heavy" isotope-labelled $^{13}C_6$ L-arginine (Arg6, Cambridge Isotopes, Cat # CLM-2265-H), 146 mg/L "heavy" isotope-labelled 4,4,5,5-D4 L-Lysine (Lys4, Cambridge Isotopes, Cat # DLM-2640). Tissue explants were cultured for 7 days in hypoxia (1% O_2 and 5% CO_2 in air) at 37^{0}C before being washed with PBS and frozen until use.

Protein extraction and preparation for cadaveric and SILAC samples

The frozen samples were pulverised using a freezer mill (Spex) under liquid nitrogen. Samples were extracted using 15 volumes (w/v) of extraction buffer (4M guanidine hydrochloride (GuHCl),

bioRxiv preprint doi: https://doi.org/10.1101/2020.07.11.192948; this version posted November 21, 2020. The copyright holder for this preprint (which was not certified by peer review) is the author/funder. All rights reserved. No reuse allowed without permission.

50 mM sodium acetate, 100 mM 6-aminocaproic acid, and HALT protease inhibitor cocktail (Thermo Fischer Scientific), pH 5.8). Samples were mechanically dissociated with 10 freeze-thaw cycles and sonicated in a cold water bath, before extraction with gentle agitation at 4°C for 48 hours. Samples were centrifuged at 15,000g for 30 minutes at 4°C and the supernatant was ethanol precipitated at a ratio of 1:9 for 16 hours at -20°C. The ethanol step was repeated and samples were centrifuged at 5000 g for 45 min at 4°C, and the protein pellets were air dried for 30 min.

Protein pellets were re-suspended in fresh 4M urea in 50 mM ammonium bicarbonate, pH 8, using water bath sonication to aid in the re-solubilisation of the samples. Samples underwent reduction with TCEP (5mM final concentration) at 60°C for 1 hr, and alkylation with iodoacetamide (500 mM final concentration) for 20 min at RT. Protein concentration was measured using the BCA assay (Biorad) according to manufacturer's instructions. 200 µg of protein was then buffer exchanged with 50 mM ammonium bicarbonate with centricon filters (Millipore, 30 kDa cutoff) according to manufacturer's instructions. Samples were digested with mass spec grade Trypsin/LysC (Promega) as per manufacturer's instructions. For SILAC-labelled samples, formic acid was added to a final concentration of 1%, and centrifuged and the supernatant then desalted prior to LC-MS/MS measurements. For the cadaveric samples, the digested peptides were then acidified with TFA (0.1% final concentration) and quantified using the peptide quantitative colorimetric peptide assay kit (Pierce, catalogue 23275) before undergoing fractionation using the High pH reversed phase peptide fractionation kit (Pierce, catalogue number 84868) into four fractions. Desalted peptides, were dried, re-suspended in 0.1% formic acid prior to LC-MS/MS measurements.

Mass spectrometry for cadaveric and SILAC samples

Samples were loaded onto the Dionex UltiMate 3000 RSLC nano Liquid Chromatography coupled to the Orbitrap Fusion Lumos Tribid Mass Spectrometer. Peptides were separated on a commercial Acclaim C18 column (75 µm internal diameter × 50 cm length, 1.9 µm particle size; Thermo). Separation was attained using a linear gradient of increasing buffer B (80% ACN and 0.1% formic acid) and declining buffer A (0.1% formic acid) at 300 nL/min. Buffer B was increased to 30% B in 210 min and ramped to 40% B in 10 min followed by a quick ramp to 95% B, where it was held for 5 min before a quick ramp back to 5% B, where it was held and the column was re-equilibrated.

bioRxiv preprint doi: https://doi.org/10.1101/2020.07.11.192948; this version posted November 21, 2020. The copyright holder for this preprint (which was not certified by peer review) is the author/funder. All rights reserved. No reuse allowed without permission.

Mass spectrometer was operated in positive polarity mode with capillary temperature of 300°C. Full survey scan resolution was set to 120 000 with an automatic gain control (AGC) target value of 2×10^6, maximum ion injection time of 30 ms, and for a scan range of 400−1500 m/z. Data acquisition was in DDA mode to automatically isolate and fragment topN multiply charged precursors according to their intensities. Spectra were obtained at 30000 MS2 resolution with AGC target of 1×10^5 and maximum ion injection time of 100 ms, 1.6 m/z isolation width, and normalised collisional energy of 31. Preceding precursor ions targeted for HCD were dynamically excluded of 50 s.

Label free quantitative data processing for cadaveric samples

Raw data were analysed using MaxQuant (v.1.6.3.3, Germany). Briefly, raw files were searched using Andromeda search engine against human UniProt protein database (20,395 entries, Oct 2018), supplemented with sequences of contaminant proteins. Andromeda search parameters for protein identification were set to a tolerance of 6 ppm for the parental peptide, and 20 ppm for fragmentation spectra and trypsin specificity allowing up to 2 miscleaved sites. Oxidation of methionine, carboxyamidomethylation of cysteines was specified as a fixed modification. Minimal required peptide length was specified at 7 amino acids. Peptides and proteins detected by at least 2 label-free quantification (LFQ) ion counts for each peptide in one of the samples were accepted, with a false discovery rate (FDR) of 1%. Proteins were quantified by normalised summed peptide intensities computed in MaxQuant with the LFQ option enabled. A total of 66 profiles were obtained: 11 locations × 3 disc levels × 2 individuals; with a median of 665 proteins (minimum 419, maximum 1920) per profile.

Data processing for SILAC samples

The high resolution, high mass accuracy mass spectrometry (MS) data obtained were processed using Proteome Discoverer (Ver 2.1), wherein data were searched using Sequest algorithm against Human UniProt database (29,900 entries, May 2016), supplemented with sequences of contaminant proteins, using the following search parameters settings: oxidized methionine (M), acetylation (Protein N-term), heavy Arginine (R6) and Lysine (K4) were selected as dynamic modifications, carboxyamidomethylation of cysteines was specified as a fixed modification, minimum peptide length of 7 amino acids was enabled, tolerance of 10 ppm for the parental

bioRxiv preprint doi: https://doi.org/10.1101/2020.07.11.192948; this version posted November 21, 2020. The copyright holder for this preprint (which was not certified by peer review) is the author/funder. All rights reserved. No reuse allowed without permission.

peptide, and 20 ppm for fragmentation spectra, and trypsin specificity allowing up to 2 miscleaved sites. Confident proteins were identified using a target-decoy approach with a reversed database, strict FDR 1% at peptide and PSM level. Newly synthesised proteins were heavy labelled with Arg6- and Lys4 and the data was expressed as the normalised protein abundance obtained from heavy (labelled)/light (un-labelled) ratio.

Degradome sample preparation, mass spectrometry and data processing

Degradome analyses was performed on NP and AF from three non-degenerated and three degenerated individuals (Table 1). Frozen tissues were pulverised as described above and prepared for TAILS as previously reported (Kleifeld et al., 2010). After extraction with SDS buffer (1% SDS, 100 mM dithiothreitol, 1X protease inhibitor in deionised water) and sonication (three cycles, 15s/cycle), the supernatant (soluble fraction) underwent reduction at 37^0C and alkylation with a final concentration of 15mM iodoacetamide for 30 min at RT. Samples were precipitated using chloroform/methanol, and the protein pellet air dried. Samples were re-suspended in 1M NaOH, quantified by nanodrop, diluted to 100mM HEPES and 4M GnHCl and pH adjusted pH6.5-7.5) prior to 6-plex TMT labelling as per manufacturer's instructions (Sixplex TMT, Cat# 90061, ThermoFisher Scientific). Equal ratios of TMT-labelled samples were pooled and methanol/chloroform precipitated. Protein pellets were air-dried and re-suspended in 200mM HEPES (pH8), and digested with trypsin (1:100 ratio) for 16 hr at 37^0C, pH 6.5 and a sample was taken for pre-TAILS. High-molecular-weight dendritic polyglycerol aldehyde polymer (ratio of 5:1 w/w polymer to sample) and $NaBH_3CN$ (to a final concentration of 80 mM) was added, incubated at 37^0C for 16 hr, followed by quenching with 100 mM ethanolamine (30 min at 37^0C) and underwent ultrafiltration (MWCO of 10,000). Collected samples were desalted, acidified to 0.1% formic acid and dried, prior to MS analysis.

Samples were analysed on a Thermo Scientific Easy nLC-1000 coupled online to a Bruker Daltonics Impact II UHR QTOF. Briefly, peptides were loaded onto a 20cm x 75µm I.D. analytical column packed with 1.8µm C18 material (Dr. Maisch GmbH, Germany) in 100% buffer A (99.9% H_2O, 0.1% formic acid) at 800 bar followed by a linear gradient elution in buffer B (99.9% acetonitrile, 0.1% formic acid) to a final 30% buffer B for a total 180 min including washing with 95% buffer B. Eluted peptides were ionized by ESI and peptide ions were subjected to tandem MS

bioRxiv preprint doi: https://doi.org/10.1101/2020.07.11.192948; this version posted November 21, 2020. The copyright holder for this preprint (which was not certified by peer review) is the author/funder. All rights reserved. No reuse allowed without permission.

analysis using a data-dependent acquisition method. A top17 method was employed, where the top 17 most intense multiply charged precursor ions were isolated for MS/MS using collision-induced-dissociation, and actively excluded for 30s.

MGF files were extracted and searched using Mascot against the UniProt Homo sapiens database, with semi-ArgC specificity, TMT6plex quantification, variable oxidation of methionine, variable acetylation of N termini, 20 ppm MS1 error tolerance, 0.05 Da MS2 error tolerance and 2 missed cleavages. Mascot .dat files were imported into Scaffold Q+S v4.4.3 for peptide identification processing to a final FDR of 1%. Quantitative values were calculated through Scaffold and used for subsequent analyses.

Transcriptomic samples: isolation, RNA extraction and data processing

AF and NP tissues from 4 individuals were cut into approximately 0.5cm^3 pieces, and put into the Dulbecco's modified Eagle's medium (DMEM) (Gibco) supplemented with 20 mM HEPES (USB), 1% penicillin-streptomycin (Gibco) and 0.4% fungizone (Gibco). The tissues were digested with 0.2% pronase (Roche) for 1 hour, and centrifuged at 200 g for 5 min to remove supernatant. AF and NP were then digested by 0.1% type II collagenase (Worthington Biochemical) for 14 hours and 0.05% type II collagenase for 8 hours, respectively. Cell suspension was filtered through a 70 µm cell strainer (BD Falcon) and centrifuged at 200 g for 5 min. The cell pellet was washed with phosphate buffered saline (PBS) and centrifuged again to remove the supernatant.RNA was then extracted from the isolated disc cells using Absolutely RNA Nanoprep Kit (Stratagene), following manufacturer’s protocol, and stored at -80°C until further processing.

The quality and quantity of total RNA were assessed on the Bioanalyzer (Agilent) using the RNA 6000 Nano total RNA assay. cDNA was generated using Affymetrix GeneChip Two-Cycle cDNA Synthesis Kit, followed by *in vitro* transcription to produce biotin-labelled cRNA. The sample was then hybridised onto the Affymetrix GeneChip Human Genome U133 Plus 2.0 Array. The array image, CEL file and other related files were generated using Affymetrix GeneChip Command Console. The experiment was conducted as a service at the Centre for PanorOmic Sciences of the University of Hong Kong.

bioRxiv preprint doi: https://doi.org/10.1101/2020.07.11.192948; this version posted November 21, 2020. The copyright holder for this preprint (which was not certified by peer review) is the author/funder. All rights reserved. No reuse allowed without permission.

CEL and other files were loaded into GeneSpring GX 10 (Agilent) software. The RMA algorithm was used for probe summation. Data were normalised with baseline transformed to median of all samples. A loose filtering based on the raw intensity values was then applied to remove background noise. Consequently, transcriptomic data with a total of 54,675 probes (corresponding to 20,887 genes) and 8 profiles were obtained.

Bioinformatics and functional analyses

The detected proteins were compared against the transcription factor (TF) database (Vaquerizas et al., 2009) and the human genome nomenclature consortium database for cell surface markers (CDs) (Braschi et al., 2019), where 77 TFs and 83 CDs were detected (Supplemental Figure S3A). Excluding missing values, the LFQ levels among the data-points range from 15.6 to 41.1, with a Gaussian-like empirical distribution (Supplemental Figure S5A). The numbers of valid values per protein were found to decline rapidly when they were sorted in descending order (Supplemental Figure S5B, upper panel). To perform principal component analyses (PCAs), only a subset of genes with sufficiently large numbers of valid values (i.e. non-missing values) were used. The cut-off for this was chosen based on a point corresponding to the steepest slope of descending order of valid protein numbers (Supplemental Figure S5B, second panel), such that the increase of valid values is slower than the increase of missing values beyond that point. Subsequently, the top 507 genes were picked representing 59.8% of all valid values. This new subset includes 12.4% of all missing values. Since the subset of data still contains some missing values, an imputation strategy was adopted employing the Multiple Imputation by Chained Equations (MICE) method and package (van Buuren and Groothuis-Oudshoorn, 2011), with a max iteration set at 50 and the default PMM method (predictive mean matching). To further ensure normality, Winsorisation was applied such that genes whose average is below 5% or above 95% of all genes were also excluded from PCA. The data was then profile-wise standardised (zero-mean and 1 standard deviation) before PCA was applied on the R platform (Team, 2013).

To assess the impact of the spatiotemporal factors on the proteomic profiles, we performed Analysis of Variance (ANOVA), correlating each protein to the age, compartments, level, and directionality. To draw the soft boundaries on the PCA plot between groups of samples, support vector machines with polynomial (degree of 2) kernel were applied using the LIBSVM package

bioRxiv preprint doi: https://doi.org/10.1101/2020.07.11.192948; this version posted November 21, 2020. The copyright holder for this preprint (which was not certified by peer review) is the author/funder. All rights reserved. No reuse allowed without permission.

(Chang and Lin, 2011) and the PCA coordinates as inputs for training. A meshed grid covering the whole PCA field was created to make prediction and draw probability contours for -0.5, 0, and 0.5 from the fitted model. Hierarchical clustering was performed with (1- correlation coefficient) as the distance metrics unless otherwise specified.

To address the problem of 'dropout' effects while avoiding extra inter-dependency introduced due to imputations, we adopted three strategies in calculating the differentially expressed proteins (DEPs), namely, by statistical testing, exclusively detected, and fold-change cutoff approaches. First, for the proteins that have over half valid values in both groups under comparison, we performed t-testing with p-values adjusted for multiple testing by the false discovery rate (FDR). Those with FDR below 0.05 were considered statistical DEPs. Second, for the proteins where one group has some valid values while the other group is completely not detected, we considered the ones with over half valid values in one group to be exclusive DEPs. For those proteins that were expressed in <50% in both groups, the ones with fold-change greater than 2 were also considered to be DEPs.

To fit the lateral and anteroposterior trends for the modules of genes identified in the young samples, a Gaussian Process Estimation (GPE) model was trained using the GauPro package in R (Team, 2013). Pathway analyses was conducted on the GSEA (Subramanian et al., 2005). Signalling proteins was compiled based on 25 Signal transduction pathways listed on KEGG (Kanehisa et al., 2019).

For transcriptomic data, we used a thresholding approach to detect DEGs (differentially expressed genes), whereby a gene was considered a DEG if the $\log_2$(fold-change) is greater than 3 and the average expression (logarithmic scale) is greater than 10 (Supplemental Figure S11E-H).

The LASSO model between MRI and proteome was trained using the R package "glmnet", wherein the 85 ECMs were first imputed for missing values in them using MICE. Nine ECMs were not imputed for too many missing values, leaving 76 for training and testing. The best value for λ was determined by cross-validations. A model was then trained on the aged MRIs (dependent variable) and aged proteome of the 76 genes (independent variable). The fitted model was then applied to the young proteome to predict MRIs of the young discs.

bioRxiv preprint doi: https://doi.org/10.1101/2020.07.11.192948; this version posted November 21, 2020. The copyright holder for this preprint (which was not certified by peer review) is the author/funder. All rights reserved. No reuse allowed without permission.

Raw data depository and software availability

The mass spectrometry proteomics data have been deposited to the ProteomeXchange Consortium via the PRIDE (Vizcaino et al., 2016) repository with the following dataset identifiers for cadaver samples (PXD017774), SILAC samples (PXD018193), and degradome samples (PXD018298000). The RAW data for the transcriptome data has been deposited on NCBI GEO with accession number GSE147383. The custom scripts for processing and analysing the data were housed at github.com/hkudclab/DIPPER. An interactive web interface for the data is available at sbms.hku.hk/dclab/DIPPER .

bioRxiv preprint doi: https://doi.org/10.1101/2020.07.11.192948; this version posted November 21, 2020. The copyright holder for this preprint (which was not certified by peer review) is the author/funder. All rights reserved. No reuse allowed without permission.

Tables

Table 1. Summary of disc samples in DIPPER.

Samples	Age	Sex	Disc level/s	Disc regions	Reason for surgery
Cadaver samples					
Young spine	16	M	L3/4, L4/5, L5/S1	NP, NP/IAF, IAF, OAF	N/A
Aged spine	59	M	L3/4, L4/5, L5/S1	NP, NP/IAF, IAF, OAF	N/A
Transcriptome samples					
YND74	17	M	L1/2	NP, OAF	Scoliosis
YND88	16	M	L1/2	NP, OAF	Scoliosis
AGD40	62	F	L4/5	NP, OAF	Degeneration
AGD45	47	M	L4/5	NP, OAF	Degeneration
SILAC samples					
YND148	19	F	L2/3	OAF	Scoliosis
YND149	15	F	L1/2	OAF	Scoliosis
YND151	15	F	L1/2	NP, OAF	Scoliosis
YND152	14	F	L1/2	NP, OAF	Scoliosis
AGD80	63	M	L4/5	NP, OAF	Degeneration
Degradome samples					
YND136	17	F	L1/2	NP, OAF	Scoliosis
YND141	20	F	L1/2	NP, OAF	Scoliosis
AGD143	53	M	L1/2	NP, OAF	Trauma
AGD62	55	F	L5/S1	NP, OAF	Degeneration
AGD65	68	F	L4/5	NP, OAF	Degeneration
AGD67	55	M	L4/5	NP, OAF	Degeneration

bioRxiv preprint doi: https://doi.org/10.1101/2020.07.11.192948; this version posted November 21, 2020. The copyright holder for this preprint (which was not certified by peer review) is the author/funder. All rights reserved. No reuse allowed without permission.

Table 2. Commonly expressed ECM and associated proteins across all 66 profiles in the spatial proteome.

Categories (Number of proteins)	**Protein names**
Core matrisome	
Collagens (13)	COL1A1/2, COL2A1, COL3A1, COL5A1, COL6A1/2/3, COL11A1/2, COL12A1, COL14A1, COL15A1
Proteoglycans (14)	ACAN, ASPN, BGN, CHAD, DCN, FMOD, HAPLN1, HSPG2, LUM, OGN, OMD, PRELP, PRG4, VCAN
Glycoproteins (34)	ABI3BP, AEBP1, CILP, CILP2, COMP, DPT, ECM2, EDIL3, EFEMP2, EMILIN1, FBN1, FGA, FGB, FN1, FNDC1, LTBP2, MATN2/3, MFGE8, MXRA5, NID2, PCOLCE, PCOLCE2, PXDN, SMOC1/2, SPARC, SRPX2, TGFBI, THBS1/2/4, TNC, TNXB
Other matrisome	
ECM affiliated proteins (10)	ANXA1/2/4/5/6, CLEC11A, CLEC3A/B, CSPG4, SEMA3C
ECM regulators (16)	A2M, CD109, CST3, F13A1, HTRA1, HTRA3, ITIH5, LOXL2/3, PLOD1, SERPINA1/3/5, SERPINE2, SERPING1, TIMP1
Secreted factors (2)	ANGPTL2, FGFBP2

bioRxiv preprint doi: https://doi.org/10.1101/2020.07.11.192948; this version posted November 21, 2020. The copyright holder for this preprint (which was not certified by peer review) is the author/funder. All rights reserved. No reuse allowed without permission.

Supplemental Tables

Supplemental Table 1. Processed data of the 66 LC-MS/MS static spatial proteome profiles, the 8 heavy-to-light ratios of the SILAC data, the 12 degradome profiles, and the 8 transcriptomic profiles.

Supplemental Table 2. Differentially expressed proteins (DEPs) among pairs of sample groups within the 33 young static spatial disc profiles.

Supplemental Table 3. Differentially expressed proteins (DEPs) among pairs of sample groups within the 33 aged static spatial disc profiles.

Supplemental Table 4. Differentially expressed proteins (DEPs) between young and aged sample groups of static spatial proteomes.

Supplemental Table 5. Significantly enriched gene ontology (GO) terms associated with proteins expressed higher in all young or all aged discs.

bioRxiv preprint doi: https://doi.org/10.1101/2020.07.11.192948; this version posted November 21, 2020. The copyright holder for this preprint (which was not certified by peer review) is the author/funder. All rights reserved. No reuse allowed without permission.

Figure legends

Figure 1. Outline of samples, workflow, MRI, and global overview of data in DIPPER.

(A) Schematic diagram showing the structure of the samples, data types, and flow of analyses in DIPPER. n is the number of individuals. N is the number of genome-wide profiles.

(B) Clinical T2-weighted MRI images (3T) of the young lumbar discs in the sagittal and transverse plane (left and right panels), T1 MRI image of the young lumbar spine (middle panel).

(C) High resolution (7T) T2-weighted MRI of the aged lower lumbar spine in sagittal (left panel) and transverse plane (right panel).

(D) Diagram showing the anatomy of the IVD and locations from where the samples were taken. VB: vertebral body; NP, nucleus pulposus; AF, annulus fibrosus; IAF: inner AF; OAF: outer AF; NP/IAF: a transition zone between NP and IAF.

(E) Venn diagrams showing the overlap of detected proteins in the four major compartments. Top panel, young and aged profiles; middle, young only; bottom, aged only.

(F) Barchart showing the numbers of proteins detected per sample, categorised into matrisome (coloured) or non-matrisome proteins (grey).

(G) Barcharts showing the composition of the matrisome and matrisome-associated proteins. Heights of bars indicate the number of proteins in each category expressed per sample. The N number in brackets indicate the aggregate number of proteins.

(H) Violin plots showing the level of sub-categories of ECMs in different compartments of the disc. The green number on top of each violin shows its median. LFQ: Label Free Quantification.

(I) Top 30 HGNC gene families for all non-matrisome proteins detected in the dataset.

(J) Violin plots showing the averaged expression levels of 10 detected histones across the disc compartments and age-groups.

(K) Scatter-plot showing the co-linearity between GAPDH and histones.

Figure 2. Principle component analysis (PCA) of the 66 static spatial profiles based on a set of 507 genes selected by optimal cut-off (see Supplemental Figure S5A-C).

(A) Scatter-plot of PC1 and PC2 color-coded by compartments, and dot-shaped by age-groups. Solid curves are the support vector machines (SVMs) decision boundaries

bioRxiv preprint doi: https://doi.org/10.1101/2020.07.11.192948; this version posted November 21, 2020. The copyright holder for this preprint (which was not certified by peer review) is the author/funder. All rights reserved. No reuse allowed without permission.

between inner disc regions (NP, NP/IAF, IAF) and OAF, and dashed curves are soft boundaries for probability equal to ±0.5 and are applied to all plots in this figure.

(B) Scatter-plot of PC1 and PC2 color-coded by disc levels. The SVM boundaries are trained between L5/S1 and upper levels (L3/4 and L4/5).

(C) Scatter-plot of PC1 and PC3, color-coded by disc compartments. The SVM boundaries are trained between inner disc regions and OAF.

(D) Scatter-plot of PC1 and PC3, color-coded by disc levels. The SVM boundaries are trained between L5/S1 and upper levels (L3/4 and L4/5).

(E) Top 100 positively and negatively correlated genes with PC1, color-coded by ECM categories.

(F) Top 100 positively and negatively correlated genes with PC2, color-coded by ECM categories.

(G) Top 100 positively and negatively correlated genes with PC3, color-coded by ECM categories.

Figure 3. Delineating the young and healthy discs' static spatial proteome.

(A) PCA plot of all 33 young profiles. Curves in the upper panel show the SVM boundaries between the OAF and inner disc regions, those in the lower panel separate the L5/S1 disc from the upper disc levels. L, left; R, right; A, anterior; P, posterior.

(B) A schematic illustrating the partitioning of the detected human disc proteome into variable and constant sets.

(C) A histogram showing the distribution of non-DEPs in terms of their detected frequencies in the young discs. Only 245 non-DEP proteins were detected in over 16 profiles, which is thus defined to be the constant set; while the remaining ~1,000 proteins were considered marginally detected.

(D) Piecharts showing the ECM compositions in the variable (left) and constant (right) sets. The constant set proteins that were detected in all 33 young profiles are listed at the bottom.

(E) Normalised expression (Z-scores) of proteins in the young module Y1 (NP signature) laterally (top panel) and anteroposterially (bottom panel), for all three disc levels combined. The red curve is the Gaussian Process Estimation (GPE) trendline, and the blue curves are 1 standard deviation above or below the trendline.

bioRxiv preprint doi: https://doi.org/10.1101/2020.07.11.192948; this version posted November 21, 2020. The copyright holder for this preprint (which was not certified by peer review) is the author/funder. All rights reserved. No reuse allowed without permission.

(F) Lateral trends of module Y2 (AF signature) for each of the three disc levels.

(G) Lateral trends of module Y3 (Smooth muscle cell signature) for each of the three disc levels.

(H) Lateral trends of module Y4 (Immune and blood) for each of the three disc levels.

(I) Volcano plot of differentially expressed proteins (DEPs) between OAF and inner disc (an aggregate of NP, NP/IAF, IAF), with coloured dots representing DEPs.

(J) A functional categorisation of the DEPs in (I).

Figure 4. Characterisation of the aged discs' static spatial proteome.

(A) PCA plot of all the aged profiles on PC1 and PC2, color-coded by compartments. Curves in the left panel show the SVM boundaries between OAF and inner disc; those in the right panel separate the L5/S1 disc from the upper disc levels. Letters on dots indicate directions: L, left; R, right; A, anterior; P, posterior.

(B) Volcano plot showing the DEPs between the OAF and inner disc (an aggregate of NP, NP/IAF and IAF), with the coloured dots representing statistically significant (FDR<0.05) DEPs.

(C) Using the same 4 modules identified in young samples, we determined the trend for these in the aged samples. Locational trends of module Y1 showing higher expression in the inner disc, albeit they are more flattened than in the young disc samples. Top panel shows left to right direction and bottom panel shows anterior to posterior direction. The red curve is the Gaussian Process Estimation (GPE) trendline, and the blue curves are 1 standard deviation above or below the trendline. This also applies to (D), (E) and (F).

(D) Lateral trends for module Y2 in the aged discs.

(E) Lateral trends for module Y3 in the aged discs.

(F) Lateral trends for module Y4 in the aged discs.

Figure 5. Comparison between young and aged static spatial proteomes.

(A) Volcano plot showing the DEPs between all the 33 young and 33 aged profiles. Coloured dots represent statistically significant DEPs.

(B) GO term enrichment of DEPs higher in young profiles.

bioRxiv preprint doi: https://doi.org/10.1101/2020.07.11.192948; this version posted November 21, 2020. The copyright holder for this preprint (which was not certified by peer review) is the author/funder. All rights reserved. No reuse allowed without permission.

(C) GO term enrichment of DEPs higher in aged profiles. Full names of GO terms in (B) and (C) are listed in Supplemental Table S5.

(D) Volcano plot showing DEPs between aged and young inner disc regions.

(E) Volcano plot showing DEPs between aged and young OAF.

(F) Venn diagram showing the partitioning of the young/aged DEPs that were down-regulated in aged discs, into contributions from inner disc regions and OAF.

(G) Venn diagram showing the partitioning of the young/aged DEPs that were up-regulated in aged discs, into contributions from inner disc regions and OAF.

(H) A heat map showing proteins expressed in all young and aged disc, with the identification of 6 modules (module 1: higher expression in young inner disc regions, modules 2 and 4: higher expression in young OAF, module 3: highly expressing in aged OAF, module 5: higher expression across all aged samples, and module 6: higher expression in aged inner disc, and some OAF).

(I) An alluvial chart showing the six modules identified in (H) and their connections to the previously identified four modules and constant set in the young reference proteome; as well as their connections to enriched GO terms.

Figure 6. Concordance between static spatial proteomic and transcriptome data.

(A) A PCA plot of the 8 transcriptomic profiles. Curves represent SVM boundaries between patient-groups or compartments.

(B) Venn diagrams showing the partitioning of the young/aged DEGs into contributions from inner disc regions and OAF. Left: down-regulated in AGD samples; right: up-regulated.

(C) Transcriptome data from the NP and AF of two young individuals were compared to the proteomic data, with coloured dots representing identified proteins also expressed at the transcriptome level.

(D) Transcriptome and proteome comparison of aged OAF and NP.

(E) Transcriptome and proteome comparison of young and aged OAF.

(F) Transcriptome and proteome comparison of young and aged NP.

bioRxiv preprint doi: https://doi.org/10.1101/2020.07.11.192948; this version posted November 21, 2020. The copyright holder for this preprint (which was not certified by peer review) is the author/funder. All rights reserved. No reuse allowed without permission.

Figure 7. The dynamic proteome of the intervertebral disc shows less biosynthesis of proteins in aged tissues.

(A) Schematic showing pulse-SILAC labelling of *ex-vivo* cultured disc tissues where heavy Arg and Lys are incorporated into newly made proteins (heavy), and pre-existing proteins remaining unlabelled (light). NP and AF tissues from young (n=3) and aged (n=1) were cultured for 7 days in hypoxia prior to MS.

(B) Barcharts showing the number of identified non-matrisome (grey) and matrisome (coloured) existing proteins (middle panel); newly synthesised proteins (left panel), and the heavy/light ratio (right panel) for each of the samples.

(C) The quantities of each of the heavy labelled (newly synthesised) proteins identified for each of the four groups were averaged, and then plotted in descending order of abundance. It shows that YND AF and NP synthesise higher numbers of proteins than the AGD AF and NP. The red dotted reference line shows the expression of GAPDH.

(D) The quantities of each of the light (existing) proteins identified for each group was averaged, and then plotted in descending order of abundance which shows that there are similar levels of existing proteins in the four pooled samples.

(E) The matrisome proteins of (C) were singled out for display. The abundance of these proteins in YND samples were generally higher across all types of matrisome proteins than the AGD, with the exceptions of aged related proteins.

(F) Schematic showing the workflow of degradome analysis by N-terminal amine isotopic labelling (TAILS) for the identification of cleaved neo N-terminal peptides.

(G) Heatmap showing the identification of cleaved proteins ranked according to tandem mass tag (TMT) isobaric labelling of N-terminal peptides in NP. Data is expressed as the $\log_2$(ratio) of N-terminal peptides.

(H) Heatmap showing the identification of cleaved proteins ranked according to tandem mass tag (TMT) isobaric labelling of N-terminal peptides in AF. Data is expressed as the $\log_2$(ratio) of N-terminal peptides. AGD143 in (G) and (H) is aged but not degenerated (trauma).

Figure 8. MRI intensities and their correlation with the proteomic data.

(A) The middle MRI stack of each disc level in the aged cadaveric sample.

(B) Schematic of the disc showing the three stacks of MRI images per disc.

bioRxiv preprint doi: https://doi.org/10.1101/2020.07.11.192948; this version posted November 21, 2020. The copyright holder for this preprint (which was not certified by peer review) is the author/funder. All rights reserved. No reuse allowed without permission.

(C) Violin plots showing the pixel intensities within each location per disc level, corresponding to the respective locations taken for mass spectrometry measurements. Each violin-plot is the aggregate of three stacks of MRIs per disc.

(D) A heatmap bi-clustering of levels and compartments based on the MRI intensities.

(E) The hydration ECMs: the ECM proteins most positively and negatively correlated with MRI.

(F) The 3T MRI intensities of the young discs across the compartments (left), and the predicted MRI intensities based on a LASSO regression model trained on the hydration ECMs (right).

(G) A water-tank model of the dynamics in disc proteomics showing the balance of the proteome is maintained by adequate anabolism to balance catabolism.

(H) Diagram showing the partitioning of the detected proteins into variable and constant sets, whereby four modules characterising the young healthy disc were further derived; and showing their changes with ageing. SMC: smooth muscle cell markers.

bioRxiv preprint doi: https://doi.org/10.1101/2020.07.11.192948; this version posted November 21, 2020. The copyright holder for this preprint (which was not certified by peer review) is the author/funder. All rights reserved. No reuse allowed without permission.

Author contributions

VT handled IRB/IC, coordinated MRI measurements, performed tissue dissection, sample preparation, data processing (MaxQuant), analyses (Perseus) and interpretation, prepared figures. PKC performed bioinformatics analyses (ANOVA, PCA, SVM, DEGs, GPE, LASSO), and prepared figures. VT and PKC wrote the first draft of the manuscript. AY generated the microarray data. RS, NS and TK performed the mass spectrometry and processed the data, supervised and funded by CMO. MK, PS and WC were involved in interpretation. LH provided the young spine and interpreted the data. KC provided critical input, interpreted results and was involved in writing. DC conceived ideas, supervised the project, interpreted data and results, wrote the manuscript. All authors contributed to writing and approved the manuscript.

Acknowledgments

We thank Dr Ed Wu and Dr Anna Wang of the Dept of EEE at HKU for performing the high-resolution MRI on the aged discs. We thank Dr Dino Samartzis for arranging the MRI of the young lumbar spine, and Prof. Kenneth Cheung and Dr Jason Cheung for collecting surgical disc specimens. Part of this work was supported by the Theme-based Research Scheme (T12-708/12N) and Area of Excellence (AoE/M-04/04) of the Hong Kong Research Grants (RGC) Council awarded to KSEC (Project Coordinator and PI) and DC (co-PI), the RGC European Union - Hong Kong Research and Innovation Cooperation Co-funding Mechanism (E-HKU703/18) awarded to DC, and by the Ministry of Science and Technology of the People's Republic of China: National Strategic Basic Research Program ("973") (2014CB942900) awarded to DC. The TAILS analyses were supported by a Canadian Institutes of Health Research Foundation Grant FDN-148408 to CMO, who holds a Canada Research Chair in Protease Proteomics and Systems Biology.

bioRxiv preprint doi: https://doi.org/10.1101/2020.07.11.192948; this version posted November 21, 2020. The copyright holder for this preprint (which was not certified by peer review) is the author/funder. All rights reserved. No reuse allowed without permission.

References

Anderson, R.M., Lawrence, A.R., Stottmann, R.W., Bachiller, D., and Klingensmith, J. (2002). Chordin and noggin promote organizing centers of forebrain development in the mouse. Development *129*, 4975-4987.

Barber, R.D., Harmer, D.W., Coleman, R.A., and Clark, B.J. (2005). GAPDH as a housekeeping gene: analysis of GAPDH mRNA expression in a panel of 72 human tissues. Physiol Genomics *21*, 389-395.

Bizet, A.A., Liu, K., Tran-Khanh, N., Saksena, A., Vorstenbosch, J., Finnson, K.W., Buschmann, M.D., and Philip, A. (2011). The TGF-beta co-receptor, CD109, promotes internalization and degradation of TGF-beta receptors. Biochim Biophys Acta *1813*, 742-753.

Braschi, B., Denny, P., Gray, K., Jones, T., Seal, R., Tweedie, S., Yates, B., and Bruford, E. (2019). Genenames.org: the HGNC and VGNC resources in 2019. Nucleic Acids Res *47*, D786-D792.

Chang, C.C., and Lin, C.J. (2011). LIBSVM: A Library for Support Vector Machines. Acm T Intel Syst Tec *2*.

Chen, J., Yan, W., and Setton, L.A. (2006). Molecular phenotypes of notochordal cells purified from immature nucleus pulposus. Eur Spine J *15 Suppl 3*, S303-311.

Dong, Y.F., Soung do, Y., Schwarz, E.M., O'Keefe, R.J., and Drissi, H. (2006). Wnt induction of chondrocyte hypertrophy through the Runx2 transcription factor. J Cell Physiol *208*, 77-86.

Feng, H., Danfelter, M., Stromqvist, B., and Heinegard, D. (2006). Extracellular matrix in disc degeneration. J Bone Joint Surg Am *88 Suppl 2*, 25-29.

Fortelny, N., Overall, C.M., Pavlidis, P., and Freue, G.V.C. (2017). Can we predict protein from mRNA levels? Nature *547*, E19-E20.

Fujita, N., Miyamoto, T., Imai, J., Hosogane, N., Suzuki, T., Yagi, M., Morita, K., Ninomiya, K., Miyamoto, K., Takaishi, H., *et al.* (2005). CD24 is expressed specifically in the nucleus pulposus of intervertebral discs. Biochem Biophys Res Commun *338*, 1890-1896.

Grimsrud, C.D., Romano, P.R., D'Souza, M., Puzas, J.E., Schwarz, E.M., Reynolds, P.R., Roiser, R.N., and O'Keefe, R.J. (2001). BMP signaling stimulates chondrocyte maturation and the expression of Indian hedgehog. J Orthop Res *19*, 18-25.

Hiyama, A., Sakai, D., Risbud, M.V., Tanaka, M., Arai, F., Abe, K., and Mochida, J. (2010). Enhancement of intervertebral disc cell senescence by WNT/beta-catenin signaling-induced matrix metalloproteinase expression. Arthritis Rheum *62*, 3036-3047.

Hou, G., Lu, H., Chen, M., Yao, H., and Zhao, H. (2014). Oxidative stress participates in age-related changes in rat lumbar intervertebral discs. Arch Gerontol Geriatr *59*, 665-669.

Humzah, M.D., and Soames, R.W. (1988). Human intervertebral disc: structure and function. Anat Rec *220*, 337-356.

Jayasuriya, C.T., Goldring, M.B., Terek, R., and Chen, Q. (2012). Matrilin-3 induction of IL-1 receptor antagonist is required for up-regulating collagen II and aggrecan and down-regulating ADAMTS-5 gene expression. Arthritis Res Ther *14*, R197.

Ji, Q., Zheng, Y., Zhang, G., Hu, Y., Fan, X., Hou, Y., Wen, L., Li, L., Xu, Y., Wang, Y., *et al.* (2019). Single-cell RNA-seq analysis reveals the progression of human osteoarthritis. Ann Rheum Dis *78*, 100-110.

Jim, J.J., Noponen-Hietala, N., Cheung, K.M., Ott, J., Karppinen, J., Sahraravand, A., Luk, K.D., Yip, S.P., Sham, P.C., Song, Y.Q., *et al.* (2005). The TRP2 allele of COL9A2 is an age-dependent risk factor for the development and severity of intervertebral disc degeneration. Spine (Phila Pa 1976) *30*, 2735-2742.

Johnson, J.L., Hall, T.E., Dyson, J.M., Sonntag, C., Ayers, K., Berger, S., Gautier, P., Mitchell, C., Hollway, G.E., and Currie, P.D. (2012). Scube activity is necessary for Hedgehog signal transduction in vivo. Dev Biol *368*, 193-202.

bioRxiv preprint doi: https://doi.org/10.1101/2020.07.11.192948; this version posted November 21, 2020. The copyright holder for this preprint (which was not certified by peer review) is the author/funder. All rights reserved. No reuse allowed without permission.

Kalamajski, S., Bihan, D., Bonna, A., Rubin, K., and Farndale, R.W. (2016). Fibromodulin Interacts with Collagen Cross-linking Sites and Activates Lysyl Oxidase. J Biol Chem *291*, 7951-7960.

Kanehisa, M., Sato, Y., Furumichi, M., Morishima, K., and Tanabe, M. (2019). New approach for understanding genome variations in KEGG. Nucleic Acids Res *47*, D590-D595.

Kleifeld, O., Doucet, A., auf dem Keller, U., Prudova, A., Schilling, O., Kainthan, R.K., Starr, A.E., Foster, L.J., Kizhakkedathu, J.N., and Overall, C.M. (2010). Isotopic labeling of terminal amines in complex samples identifies protein N-termini and protease cleavage products. Nat Biotechnol *28*, 281-288.

Komori, T. (2010). Regulation of bone development and extracellular matrix protein genes by RUNX2. Cell Tissue Res *339*, 189-195.

Lam, T.-k. (2013). Fate of notochord descendent cells in the intervertebral disc. In HKU Theses Online (HKUTO) (The University of Hong Kong (Pokfulam, Hong Kong)).

Lau, D., Elezagic, D., Hermes, G., Morgelin, M., Wohl, A.P., Koch, M., Hartmann, U., Hollriegl, S., Wagener, R., Paulsson, M., *et al.* (2018). The cartilage-specific lectin C-type lectin domain family 3 member A (CLEC3A) enhances tissue plasminogen activator-mediated plasminogen activation. J Biol Chem *293*, 203-214.

Lee, C.G., Da Silva, C.A., Dela Cruz, C.S., Ahangari, F., Ma, B., Kang, M.J., He, C.H., Takyar, S., and Elias, J.A. (2011). Role of chitin and chitinase/chitinase-like proteins in inflammation, tissue remodeling, and injury. Annu Rev Physiol *73*, 479-501.

Leijten, J.C., Bos, S.D., Landman, E.B., Georgi, N., Jahr, H., Meulenbelt, I., Post, J.N., van Blitterswijk, C.A., and Karperien, M. (2013). GREM1, FRZB and DKK1 mRNA levels correlate with osteoarthritis and are regulated by osteoarthritis-associated factors. Arthritis Res Ther *15*, R126.

Li, C., Hancock, M.A., Sehgal, P., Zhou, S., Reinhardt, D.P., and Philip, A. (2016). Soluble CD109 binds TGF-beta and antagonizes TGF-beta signalling and responses. Biochem J *473*, 537-547.

Lopez-Otin, C., and Overall, C.M. (2002). Protease degradomics: a new challenge for proteomics. Nat Rev Mol Cell Biol *3*, 509-519.

Lu, Y., Qiao, L., Lei, G., Mira, R.R., Gu, J., and Zheng, Q. (2014). Col10a1 gene expression and chondrocyte hypertrophy during skeletal development and disease. Frontiers in Biology *9*, 195-204.

Markmann, A., Hausser, H., Schonherr, E., and Kresse, H. (2000). Influence of decorin expression on transforming growth factor-beta-mediated collagen gel retraction and biglycan induction. Matrix Biol *19*, 631-636.

Maseda, M., Yamaguchi, H., Kuroda, K., Mitsumata, M., Tokuhashi, Y., and Esumi, M. (2016). Proteomic Analysis of Human Intervertebral Disc Degeneration. Journal of Nihon University Medical Association *75*, 16-21.

Melas, I.N., Chairakaki, A.D., Chatzopoulou, E.I., Messinis, D.E., Katopodi, T., Pliaka, V., Samara, S., Mitsos, A., Dailiana, Z., Kollia, P., *et al.* (2014). Modeling of signaling pathways in chondrocytes based on phosphoproteomic and cytokine release data. Osteoarthritis Cartilage *22*, 509-518.

Minogue, B.M., Richardson, S.M., Zeef, L.A., Freemont, A.J., and Hoyland, J.A. (2010). Characterization of the human nucleus pulposus cell phenotype and evaluation of novel marker gene expression to define adult stem cell differentiation. Arthritis Rheum *62*, 3695-3705.

Molinos, M., Almeida, C.R., Caldeira, J., Cunha, C., Goncalves, R.M., and Barbosa, M.A. (2015). Inflammation in intervertebral disc degeneration and regeneration. J R Soc Interface *12*, 20150429.

Munir, S., Rade, M., Maatta, J.H., Freidin, M.B., and Williams, F.M.K. (2018). Intervertebral Disc Biology: Genetic Basis of Disc Degeneration. Curr Mol Biol Rep *4*, 143-150.

Naba, A., Clauser, K.R., Hoersch, S., Liu, H., Carr, S.A., and Hynes, R.O. (2012). The matrisome: in silico definition and in vivo characterization by proteomics of normal and tumor extracellular matrices. Mol Cell Proteomics *11*, M111 014647.

Nakai, T., Sakai, D., Nakamura, Y., Nukaga, T., Grad, S., Li, Z., Alini, M., Chan, D., Masuda, K., Ando, K., *et al.* (2016). CD146 defines commitment of cultured annulus fibrosus cells to express a contractile phenotype. J Orthop Res *34*, 1361-1372.

bioRxiv preprint doi: https://doi.org/10.1101/2020.07.11.192948; this version posted November 21, 2020. The copyright holder for this preprint (which was not certified by peer review) is the author/funder. All rights reserved. No reuse allowed without permission.

Nakamichi, R., Kataoka, K., and Asahara, H. (2018). Essential role of Mohawk for tenogenic tissue homeostasis including spinal disc and periodontal ligament. Mod Rheumatol *28*, 933-940.

Naveau, S., Poynard, T., Benattar, C., Bedossa, P., and Chaput, J.C. (1994). Alpha-2-macroglobulin and hepatic fibrosis. Diagnostic interest. Dig Dis Sci *39*, 2426-2432.

Nerlich, A.G., Schaaf, R., Walchli, B., and Boos, N. (2007). Temporo-spatial distribution of blood vessels in human lumbar intervertebral discs. Eur Spine J *16*, 547-555.

Newell, N., Little, J.P., Christou, A., Adams, M.A., Adam, C.J., and Masouros, S.D. (2017). Biomechanics of the human intervertebral disc: A review of testing techniques and results. J Mech Behav Biomed Mater *69*, 420-434.

Ong, S.E., Blagoev, B., Kratchmarova, I., Kristensen, D.B., Steen, H., Pandey, A., and Mann, M. (2002). Stable isotope labeling by amino acids in cell culture, SILAC, as a simple and accurate approach to expression proteomics. Mol Cell Proteomics *1*, 376-386.

Onnerfjord, P., Khabut, A., Reinholt, F.P., Svensson, O., and Heinegard, D. (2012a). Quantitative proteomic analysis of eight cartilaginous tissues reveals characteristic differences as well as similarities between subgroups. J Biol Chem *287*, 18913-18924.

Onnerfjord, P., Khabut, A., Reinholt, F.P., Svensson, O., and Heinegard, D. (2012b). Quantitative proteomic analysis of eight cartilaginous tissues reveals characteristic differences as well as similarities between subgroups. Journal of Biological Chemistry *287*, 18913-18924.

Park, J.S., Chu, J.S., Tsou, A.D., Diop, R., Tang, Z., Wang, A., and Li, S. (2011). The effect of matrix stiffness on the differentiation of mesenchymal stem cells in response to TGF-beta. Biomaterials *32*, 3921-3930.

Peix, L., Evans, I.C., Pearce, D.R., Simpson, J.K., Maher, T.M., and McAnulty, R.J. (2018). Diverse functions of clusterin promote and protect against the development of pulmonary fibrosis. Sci Rep *8*, 1906.

Pfirrmann, C.W., Metzdorf, A., Zanetti, M., Hodler, J., and Boos, N. (2001). Magnetic resonance classification of lumbar intervertebral disc degeneration. Spine (Phila Pa 1976) *26*, 1873-1878.

Rajasekaran, S., Tangavel, C., K, S.S., Soundararajan, D.C.R., Nayagam, S.M., Matchado, M.S., Raveendran, M., Shetty, A.P., Kanna, R.M., and Dharmalingam, K. (2020). Inflammaging determines health and disease in lumbar discs-evidence from differing proteomic signatures of healthy, aging, and degenerating discs. Spine J *20*, 48-59.

Rajesh, D., and Dahia, C.L. (2018). Role of Sonic Hedgehog Signaling Pathway in Intervertebral Disc Formation and Maintenance. Curr Mol Biol Rep *4*, 173-179.

Ranjani, V., Sreemol, G., Muthurajan, R., Natesan, S., Gnanam, R., Kanna, R.M., and Rajasekaran, S. (2016). Proteomic Analysis of Degenerated Intervertebral Disc-identification of Biomarkers of Degenerative Disc Disease and Development of Proteome Database. Global Spine Journal *6*, WO025.

Rauniyar, N., and Yates, J.R., 3rd (2014). Isobaric labeling-based relative quantification in shotgun proteomics. J Proteome Res *13*, 5293-5309.

Riester, S.M., Lin, Y., Wang, W., Cong, L., Mohamed Ali, A.M., Peck, S.H., Smith, L.J., Currier, B.L., Clark, M., Huddleston, P., *et al.* (2018). RNA sequencing identifies gene regulatory networks controlling extracellular matrix synthesis in intervertebral disk tissues. J Orthop Res *36*, 1356-1369.

Risbud, M.V., Schoepflin, Z.R., Mwale, F., Kandel, R.A., Grad, S., Iatridis, J.C., Sakai, D., and Hoyland, J.A. (2015). Defining the phenotype of young healthy nucleus pulposus cells: recommendations of the Spine Research Interest Group at the 2014 annual ORS meeting. J Orthop Res *33*, 283-293.

Robinson, K.A., Sun, M., Barnum, C.E., Weiss, S.N., Huegel, J., Shetye, S.S., Lin, L., Saez, D., Adams, S.M., Iozzo, R.V., *et al.* (2017). Decorin and biglycan are necessary for maintaining collagen fibril structure, fiber realignment, and mechanical properties of mature tendons. Matrix Biol *64*, 81-93.

Rodrigues-Pinto, R., Berry, A., Piper-Hanley, K., Hanley, N., Richardson, S.M., and Hoyland, J.A. (2016). Spatiotemporal analysis of putative notochordal cell markers reveals CD24 and keratins 8, 18, and 19 as notochord-specific markers during early human intervertebral disc development. J Orthop Res *34*, 1327-1340.

bioRxiv preprint doi: https://doi.org/10.1101/2020.07.11.192948; this version posted November 21, 2020. The copyright holder for this preprint (which was not certified by peer review) is the author/funder. All rights reserved. No reuse allowed without permission.

Rodriguez, A.G., Slichter, C.K., Acosta, F.L., Rodriguez-Soto, A.E., Burghardt, A.J., Majumdar, S., and Lotz, J.C. (2011). Human disc nucleus properties and vertebral endplate permeability. Spine (Phila Pa 1976) *36*, 512-520.

Rubin, D.I. (2007). Epidemiology and risk factors for spine pain. Neurol Clin *25*, 353-371.

Rutges, J.P., Duit, R.A., Kummer, J.A., Oner, F.C., van Rijen, M.H., Verbout, A.J., Castelein, R.M., Dhert, W.J., and Creemers, L.B. (2010). Hypertrophic differentiation and calcification during intervertebral disc degeneration. Osteoarthritis Cartilage *18*, 1487-1495.

Saito, T., Ikeda, T., Nakamura, K., Chung, U.I., and Kawaguchi, H. (2007). S100A1 and S100B, transcriptional targets of SOX trio, inhibit terminal differentiation of chondrocytes. EMBO Rep *8*, 504-509.

Sakai, D., Nakamura, Y., Nakai, T., Mishima, T., Kato, S., Grad, S., Alini, M., Risbud, M.V., Chan, D., Cheah, K.S., *et al.* (2012). Exhaustion of nucleus pulposus progenitor cells with ageing and degeneration of the intervertebral disc. Nat Commun *3*, 1264.

Saleem, S., Aslam, H.M., Rehmani, M.A., Raees, A., Alvi, A.A., and Ashraf, J. (2013). Lumbar disc degenerative disease: disc degeneration symptoms and magnetic resonance image findings. Asian Spine J *7*, 322-334.

Sarath Babu, N., Krishnan, S., Brahmendra Swamy, C.V., Venkata Subbaiah, G.P., Gurava Reddy, A.V., and Idris, M.M. (2016). Quantitative proteomic analysis of normal and degenerated human intervertebral disc. Spine J *16*, 989-1000.

Schneiderman, G., Flannigan, B., Kingston, S., Thomas, J., Dillin, W.H., and Watkins, R.G. (1987). Magnetic resonance imaging in the diagnosis of disc degeneration: correlation with discography. Spine (Phila Pa 1976) *12*, 276-281.

Silagi, E.S., Shapiro, I.M., and Risbud, M.V. (2018). Glycosaminoglycan synthesis in the nucleus pulposus: Dysregulation and the pathogenesis of disc degeneration. Matrix Biol *71-72*, 368-379.

Song, Y.Q., Cheung, K.M., Ho, D.W., Poon, S.C., Chiba, K., Kawaguchi, Y., Hirose, Y., Alini, M., Grad, S., Yee, A.F., *et al.* (2008). Association of the asporin D14 allele with lumbar-disc degeneration in Asians. Am J Hum Genet *82*, 744-747.

Song, Y.Q., Karasugi, T., Cheung, K.M., Chiba, K., Ho, D.W., Miyake, A., Kao, P.Y., Sze, K.L., Yee, A., Takahashi, A., *et al.* (2013). Lumbar disc degeneration is linked to a carbohydrate sulfotransferase 3 variant. J Clin Invest *123*, 4909-4917.

Subramanian, A., and Schilling, T.F. (2014). Thrombospondin-4 controls matrix assembly during development and repair of myotendinous junctions. Elife *3*.

Subramanian, A., Tamayo, P., Mootha, V.K., Mukherjee, S., Ebert, B.L., Gillette, M.A., Paulovich, A., Pomeroy, S.L., Golub, T.R., Lander, E.S., *et al.* (2005). Gene set enrichment analysis: a knowledge-based approach for interpreting genome-wide expression profiles. Proc Natl Acad Sci U S A *102*, 15545-15550.

Sun, Z., Liu, B., and Luo, Z.J. (2020). The Immune Privilege of the Intervertebral Disc: Implications for Intervertebral Disc Degeneration Treatment. Int J Med Sci *17*, 685-692.

Taha, I.N., and Naba, A. (2019). Exploring the extracellular matrix in health and disease using proteomics. Essays Biochem *63*, 417-432.

Takao, T., and Iwaki, T. (2002). A comparative study of localization of heat shock protein 27 and heat shock protein 72 in the developmental and degenerative intervertebral discs. Spine (Phila Pa 1976) *27*, 361-368.

Taye, N., Karoulias, S.Z., and Hubmacher, D. (2020). The "other" 15-40%: The Role of Non-Collagenous Extracellular Matrix Proteins and Minor Collagens in Tendon. J Orthop Res *38*, 23-35.

Team, R.C. (2013). R: A language and environment for statistical computing.

Teraguchi, M., Yoshimura, N., Hashizume, H., Muraki, S., Yamada, H., Minamide, A., Oka, H., Ishimoto, Y., Nagata, K., Kagotani, R., *et al.* (2014). Prevalence and distribution of intervertebral disc degeneration over the entire spine in a population-based cohort: the Wakayama Spine Study. Osteoarthritis Cartilage *22*, 104-110.

Tibshirani, R. (1996). Regression shrinkage and selection via the Lasso. J Roy Stat Soc B Met *58*, 267-288.

bioRxiv preprint doi: https://doi.org/10.1101/2020.07.11.192948; this version posted November 21, 2020. The copyright holder for this preprint (which was not certified by peer review) is the author/funder. All rights reserved. No reuse allowed without permission.

Trougakos, I.P. (2013). The molecular chaperone apolipoprotein J/clusterin as a sensor of oxidative stress: implications in therapeutic approaches - a mini-review. Gerontology *59*, 514-523.

Urban, J.P., Smith, S., and Fairbank, J.C. (2004). Nutrition of the intervertebral disc. Spine (Phila Pa 1976) *29*, 2700-2709.

van Buuren, S., and Groothuis-Oudshoorn, K. (2011). mice: Multivariate Imputation by Chained Equations in R. J Stat Softw *45*, 1-67.

van den Akker, G.G.H., Koenders, M.I., van de Loo, F.A.J., van Lent, P., Blaney Davidson, E., and van der Kraan, P.M. (2017). Transcriptional profiling distinguishes inner and outer annulus fibrosus from nucleus pulposus in the bovine intervertebral disc. Eur Spine J *26*, 2053-2062.

van der Kraan, P.M., and van den Berg, W.B. (2012). Chondrocyte hypertrophy and osteoarthritis: role in initiation and progression of cartilage degeneration? Osteoarthritis Cartilage *20*, 223-232.

Vaquerizas, J.M., Kummerfeld, S.K., Teichmann, S.A., and Luscombe, N.M. (2009). A census of human transcription factors: function, expression and evolution. Nat Rev Genet *10*, 252-263.

Veras, M.A., McCann, M.R., Tenn, N.A., and Seguin, C.A. (2020). Transcriptional profiling of the murine intervertebral disc and age-associated changes in the nucleus pulposus. Connect Tissue Res *61*, 63-81.

Vizcaino, J.A., Csordas, A., del-Toro, N., Dianes, J.A., Griss, J., Lavidas, I., Mayer, G., Perez-Riverol, Y., Reisinger, F., Ternent, T., *et al.* (2016). 2016 update of the PRIDE database and its related tools. Nucleic Acids Res *44*, D447-456.

Wang, X.L., Hou, L., Zhao, C.G., Tang, Y., Zhang, B., Zhao, J.Y., and Wu, Y.B. (2019a). Screening of genes involved in epithelial-mesenchymal transition and differential expression of complement-related genes induced by PAX2 in renal tubules. Nephrology (Carlton) *24*, 263-271.

Wang, Y., Fan, X., Xing, L., and Tian, F. (2019b). Wnt signaling: a promising target for osteoarthritis therapy. Cell Commun Signal *17*, 97.

Wisniewski, J.R., Hein, M.Y., Cox, J., and Mann, M. (2014). A "proteomic ruler" for protein copy number and concentration estimation without spike-in standards. Mol Cell Proteomics *13*, 3497-3506.

Wuertz, K., Vo, N., Kletsas, D., and Boos, N. (2012). Inflammatory and catabolic signalling in intervertebral discs: the roles of NF-kappaB and MAP kinases. Eur Cell Mater *23*, 103-119; discussion 119-120.

Wyatt, A.R., Yerbury, J.J., and Wilson, M.R. (2009). Structural characterization of clusterin-chaperone client protein complexes. J Biol Chem *284*, 21920-21927.

Yates, B., Braschi, B., Gray, K.A., Seal, R.L., Tweedie, S., and Bruford, E.A. (2017). Genenames.org: the HGNC and VGNC resources in 2017. Nucleic Acids Res *45*, D619-D625.

Yee, A., Lam, M.P., Tam, V., Chan, W.C., Chu, I.K., Cheah, K.S., Cheung, K.M., and Chan, D. (2016). Fibrotic-like changes in degenerate human intervertebral discs revealed by quantitative proteomic analysis. Osteoarthritis Cartilage *24*, 503-513.

Zhu, M., Tang, D., Wu, Q., Hao, S., Chen, M., Xie, C., Rosier, R.N., O'Keefe, R.J., Zuscik, M., and Chen, D. (2009). Activation of beta-catenin signaling in articular chondrocytes leads to osteoarthritis-like phenotype in adult beta-catenin conditional activation mice. J Bone Miner Res *24*, 12-21.

Zhu, S., Qiu, H., Bennett, S., Kuek, V., Rosen, V., Xu, H., and Xu, J. (2019). Chondromodulin-1 in health, osteoarthritis, cancer, and heart disease. Cell Mol Life Sci *76*, 4493-4502.

FIGURE 1

bioRxiv preprint doi: https://doi.org/10.1101/2020.07.11.192948 This version posted November 16, 2020. The copyright holder for this preprint (which was not certified by peer review) is the author/funder. All rights reserved. Used without permission.

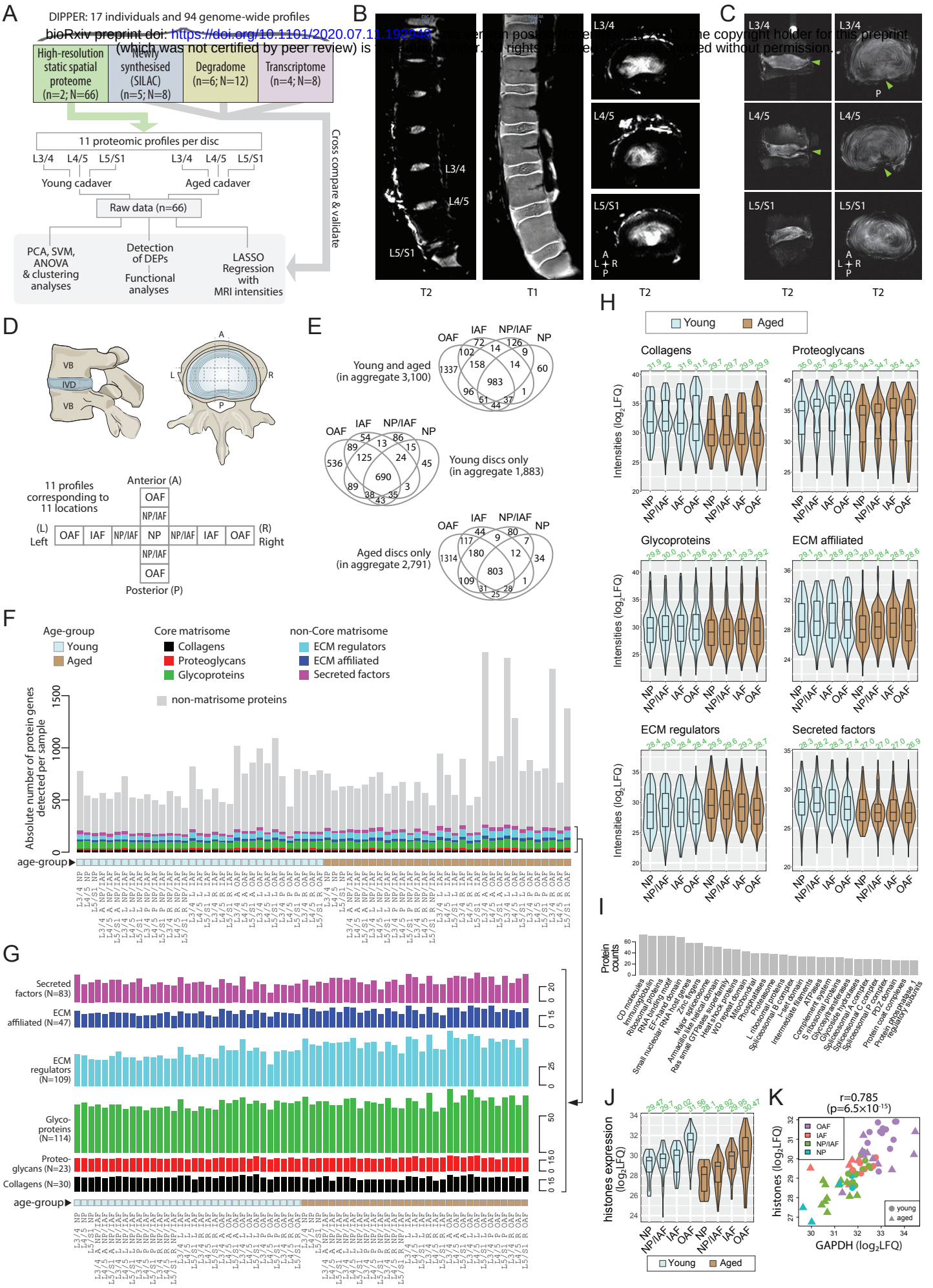

FIGURE 2

bioRxiv preprint doi: https://doi.org/10.1101/2020.07.[illegible]1.192948; this version posted November 21, 2020. The copyright holder for this preprint (which was not certified by peer review) is the author/funder. All rights reserved. No reuse allowed without permission.

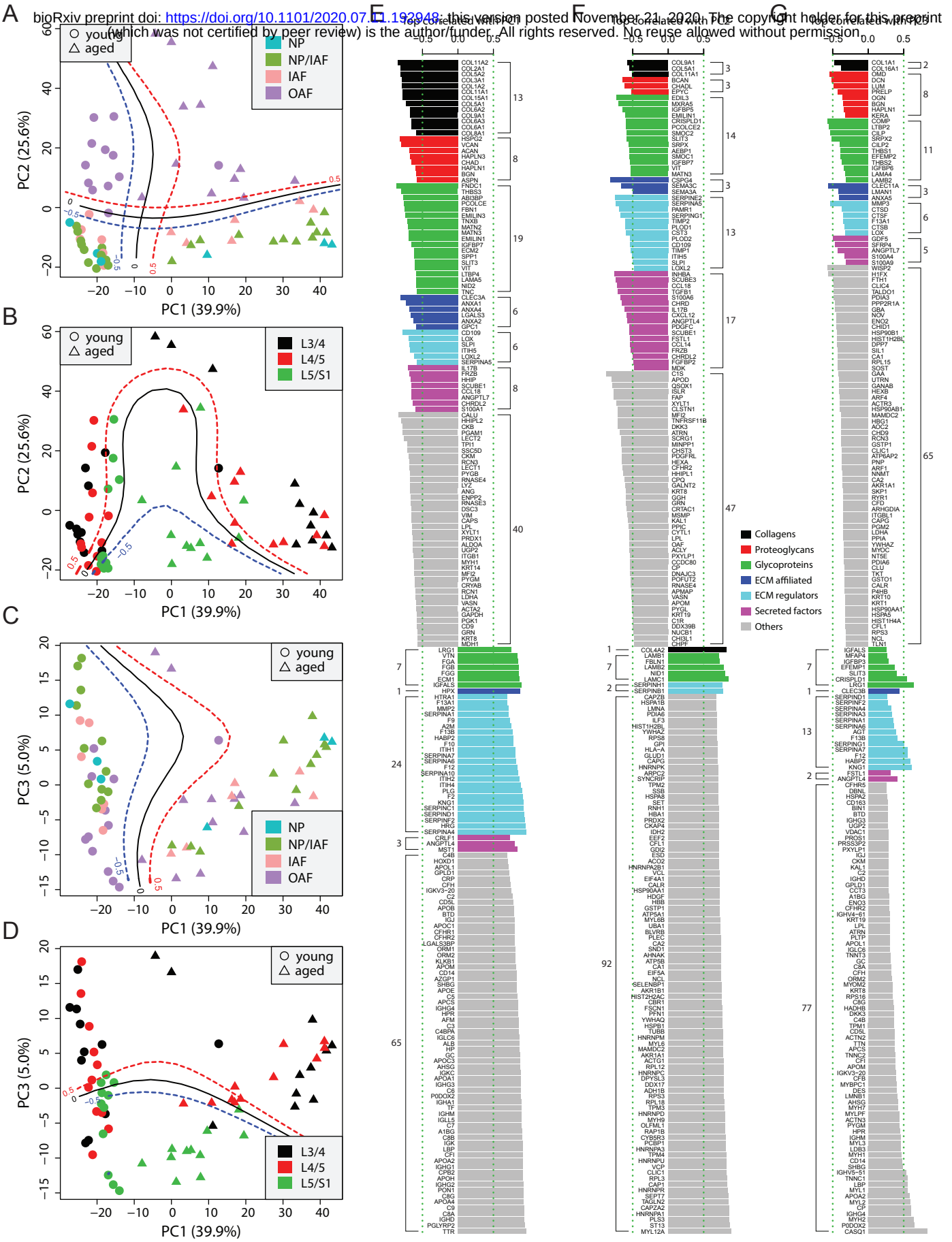

FIGURE 3

bioRxiv preprint doi: https://doi.org/10.1101/2020.07.11.192948; this version posted November 21, 2020. The copyright holder for this preprint (which was not certified by peer review) is the author/funder. All rights reserved. No reuse allowed without permission.

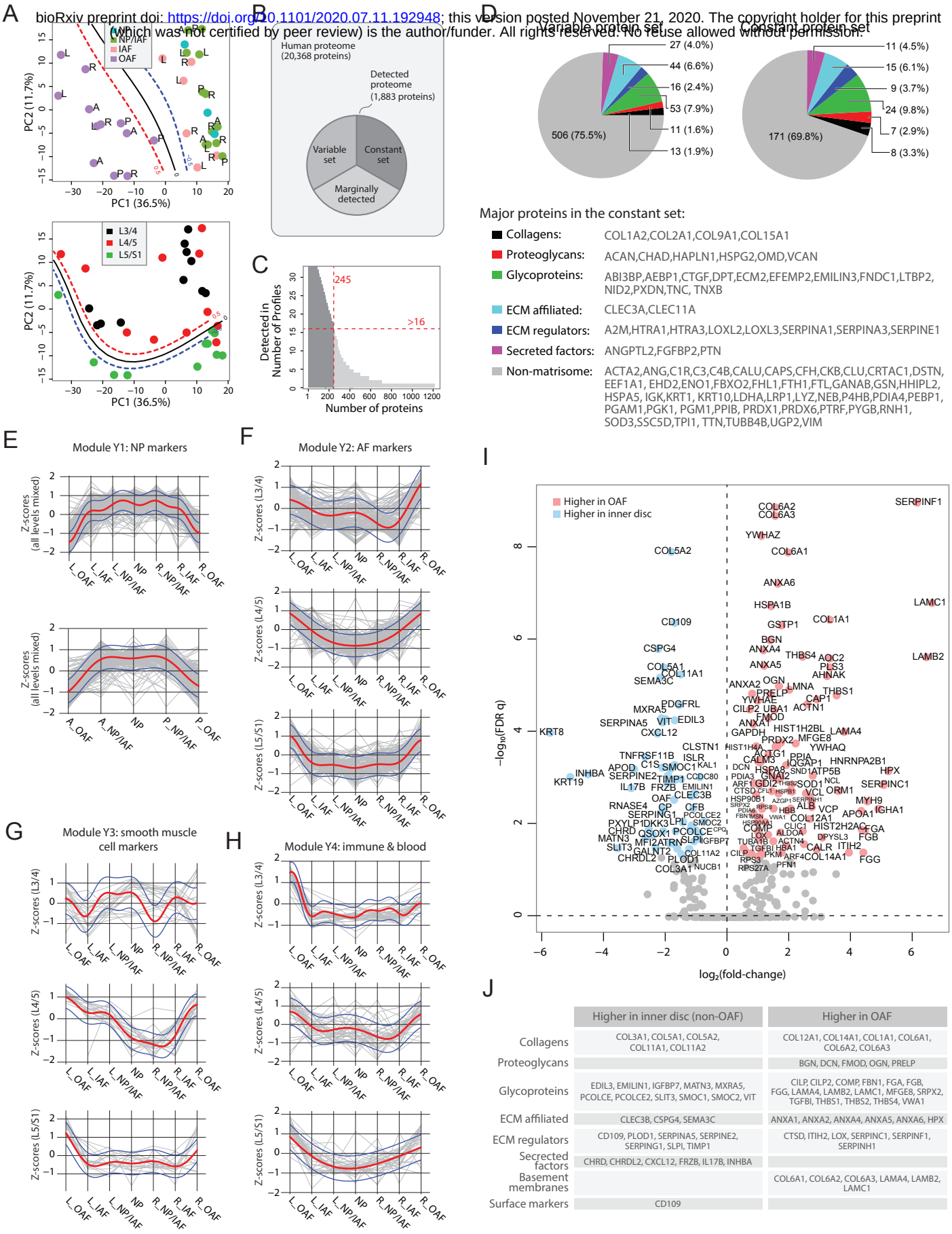

	Higher in inner disc (non-OAF)	Higher in OAF
Collagens	COL3A1, COL5A1, COL5A2, COL11A1, COL11A2	COL12A1, COL14A1, COL1A1, COL6A1, COL6A2, COL6A3
Proteoglycans		BGN, DCN, FMOD, OGN, PRELP
Glycoproteins	EDIL3, EMILIN1, IGFBP7, MATN3, MXRA5, PCOLCE, PCOLCE2, SLIT3, SMOC1, SMOC2, VIT	CILP, CILP2, COMP, FBN1, FGA, FGB, FGG, LAMA4, LAMB2, LAMC1, MFGE8, SRPX2, TGFBI, THBS1, THBS2, THBS4, VWA1
ECM affiliated	CLEC3B, CSPG4, SEMA3C	ANXA1, ANXA2, ANXA4, ANXA5, ANXA6, HPX
ECM regulators	CD109, PLOD1, SERPINA5, SERPINE2, SERPING1, SLPI, TIMP1	CTSD, ITIH2, LOX, SERPINC1, SERPINF1, SERPINH1
Secreted factors	CHRD, CHRDL2, CXCL12, FRZB, IL17B, INHBA	
Basement membranes		COL6A1, COL6A2, COL6A3, LAMA4, LAMB2, LAMC1
Surface markers	CD109	

FIGURE 4

bioRxiv preprint doi: https://doi.org/10.1101/2020.07.11.192948; this version posted November 21, 2020. The copyright holder for this preprint (which was not certified by peer review) is the author/funder. All rights reserved. No reuse allowed without permission.

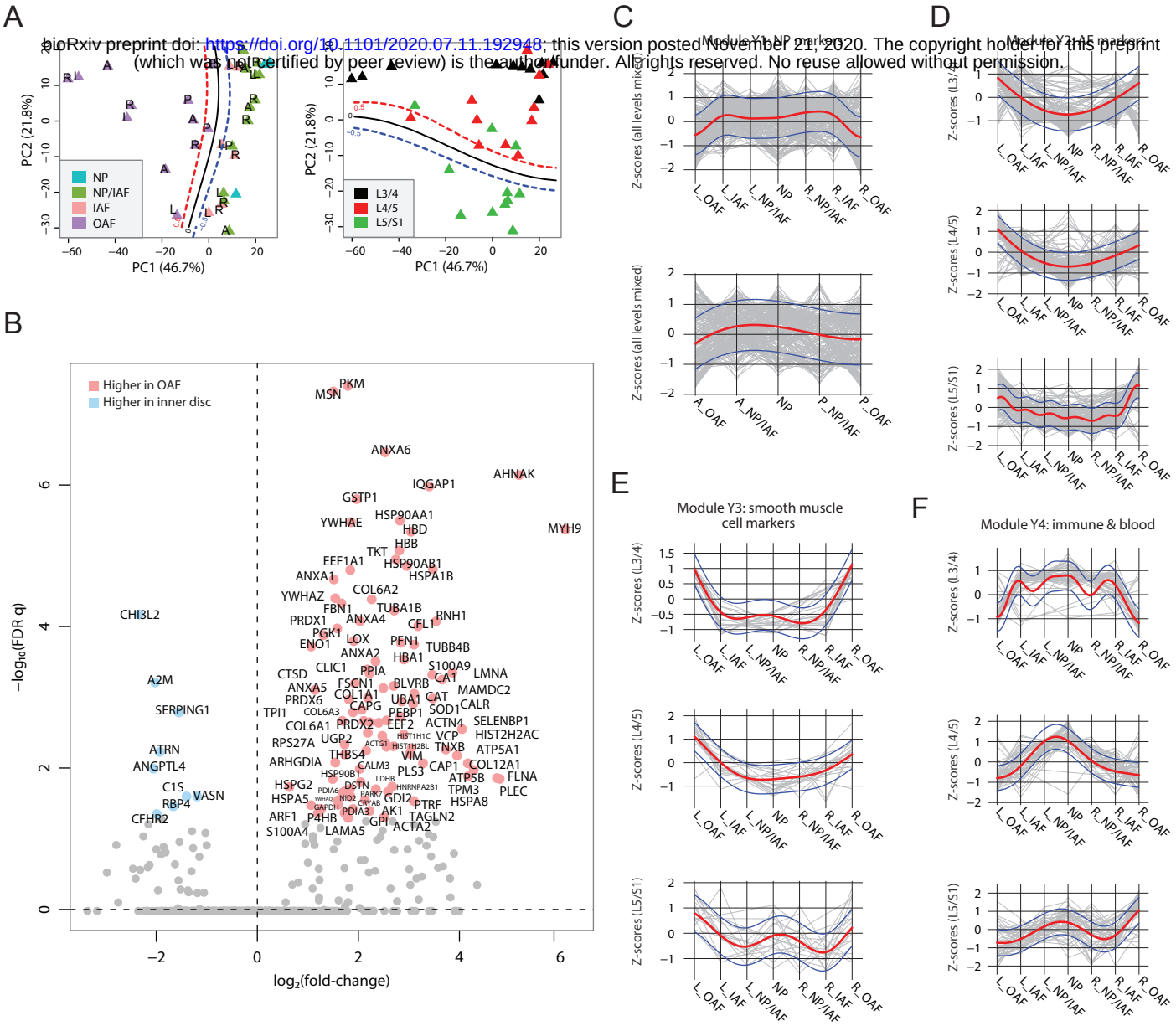

FIGURE 5

bioRxiv preprint doi: https://doi.org/10.1101/2020.07.11.192948; this version posted November 21, 2020. The copyright holder for this preprint (which was not certified by peer review) is the author/funder. All rights reserved. No reuse allowed without permission.

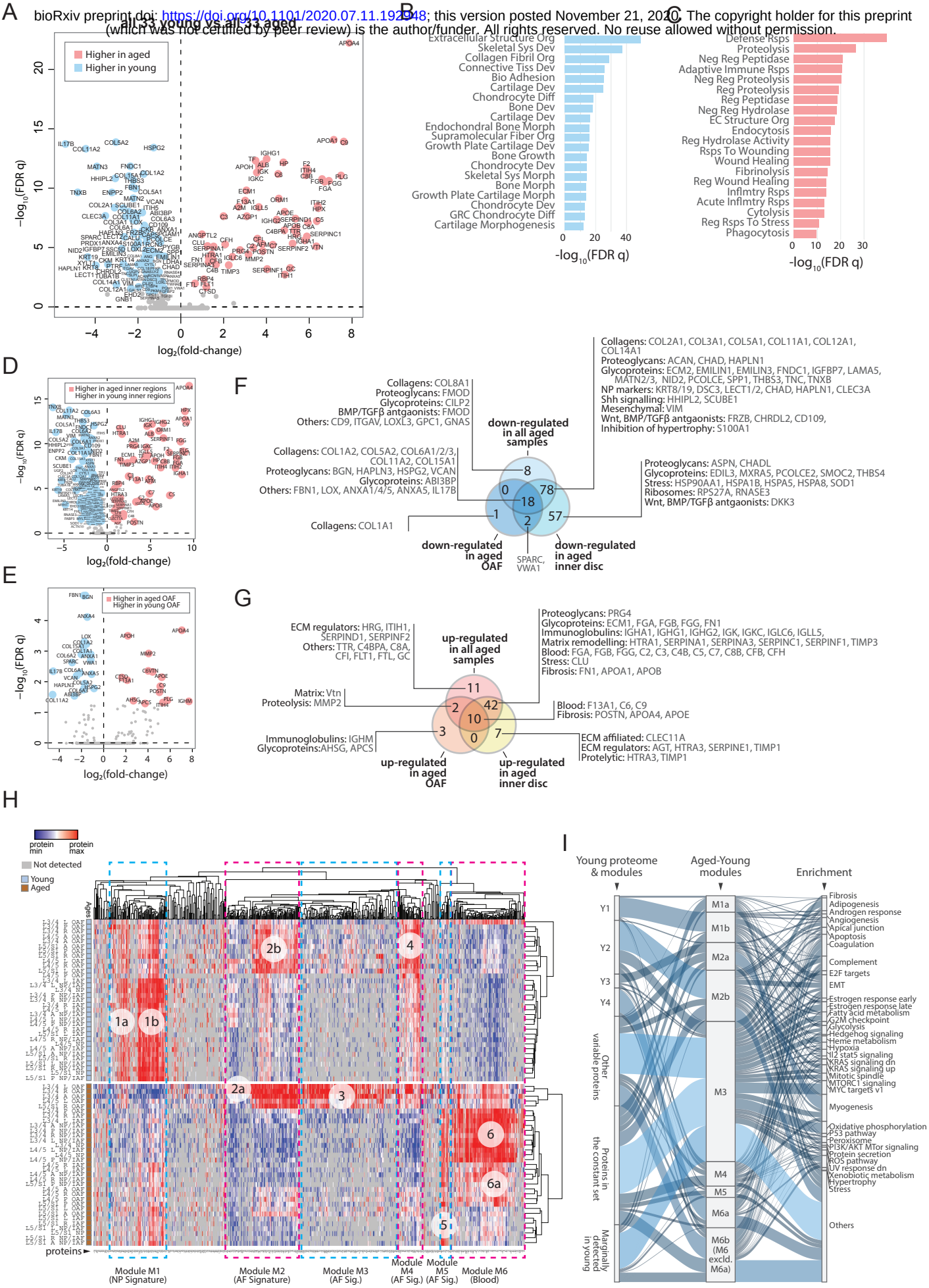

FIGURE 6

bioRxiv preprint doi: https://doi.org/10.1101/2020.07.11.192948; this version posted November 21, 2020. The copyright holder for this preprint (which was not certified by peer review) is the author/funder. All rights reserved. No reuse allowed without permission.

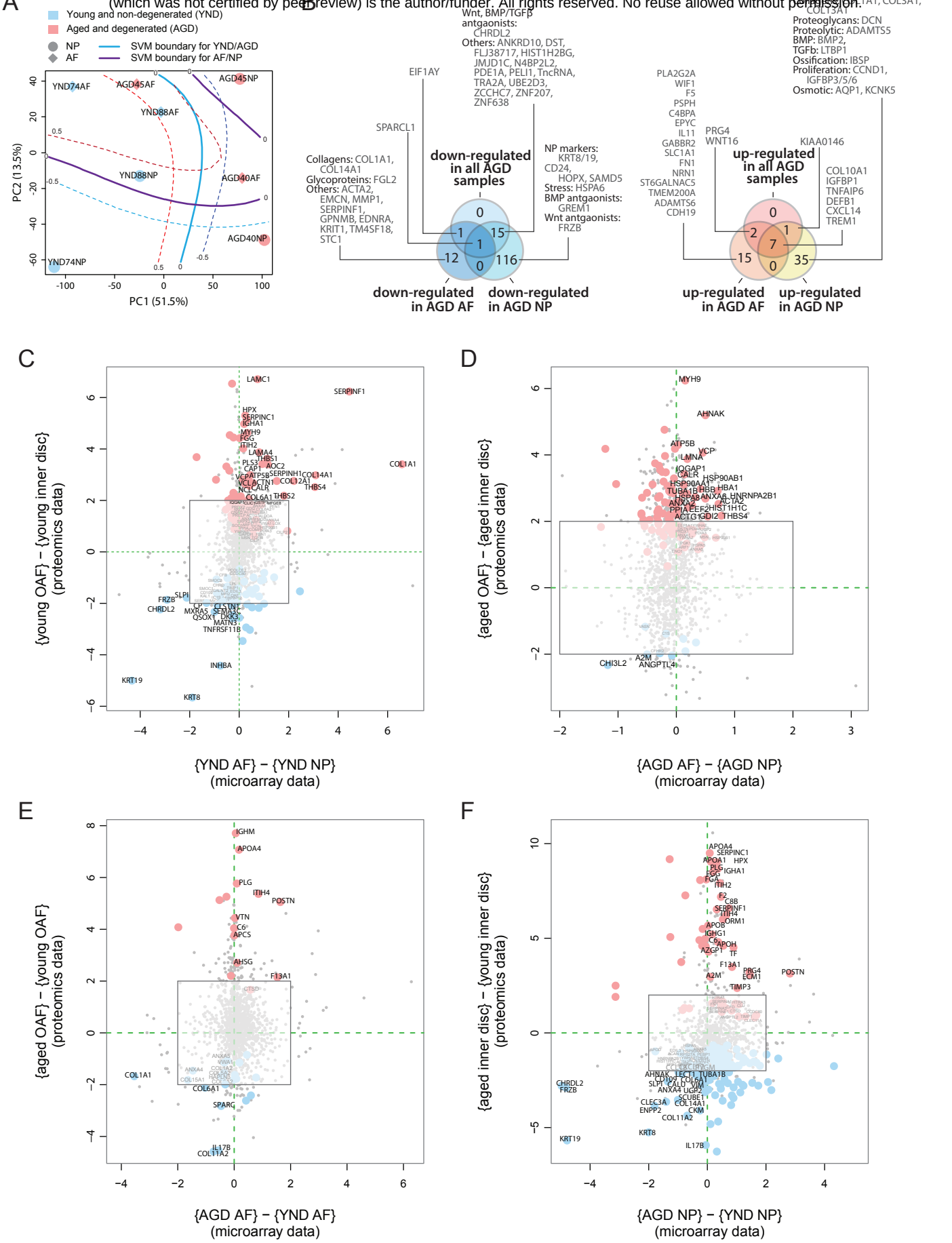

FIGURE 7

bioRxiv preprint doi: https://doi.org/10.1101/2020.07.11.198948; this version posted November 21, 2020. The copyright holder for this preprint (which was not certified by peer review) is the author/funder. All rights reserved. No reuse allowed without permission.

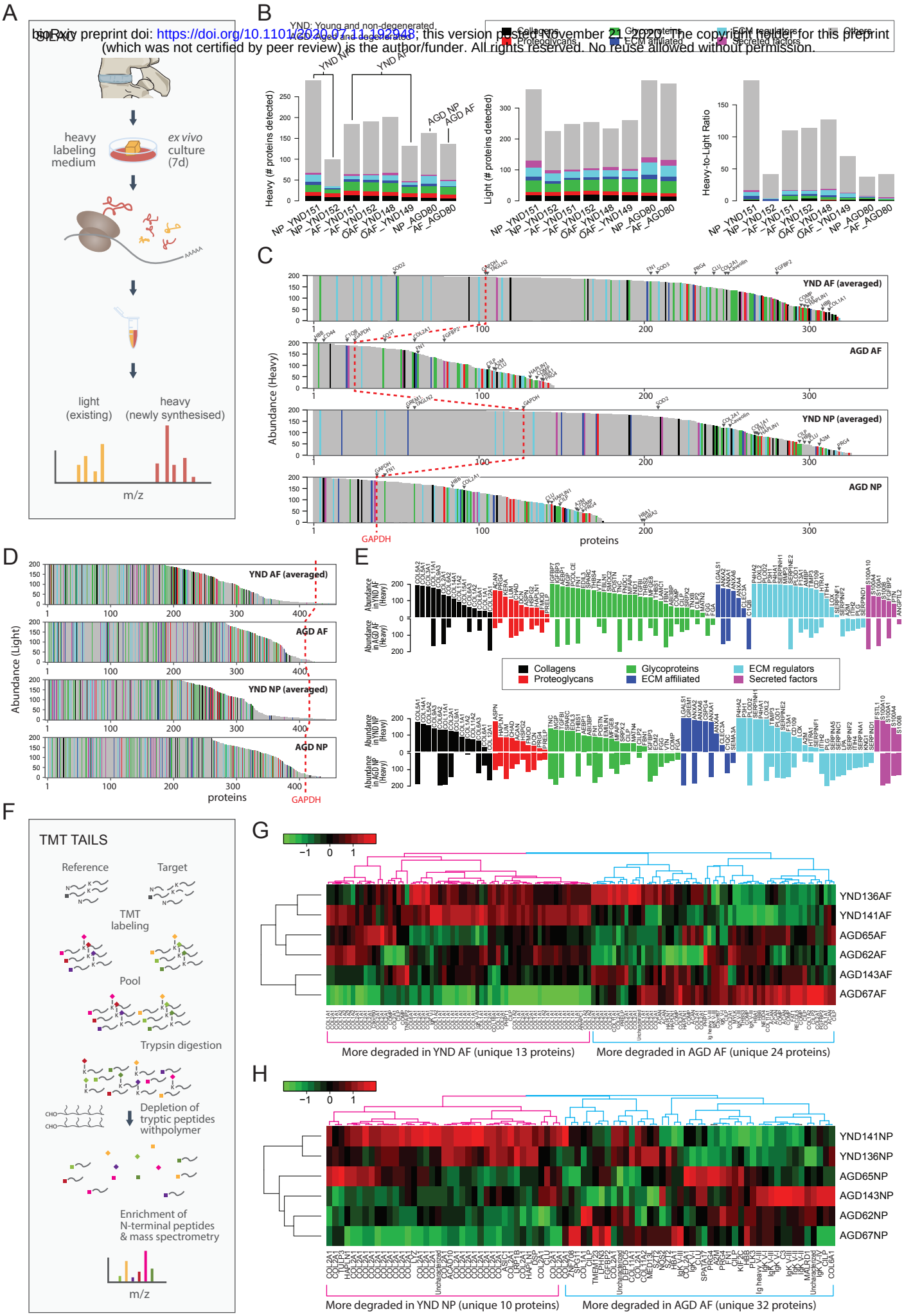

FIGURE 8
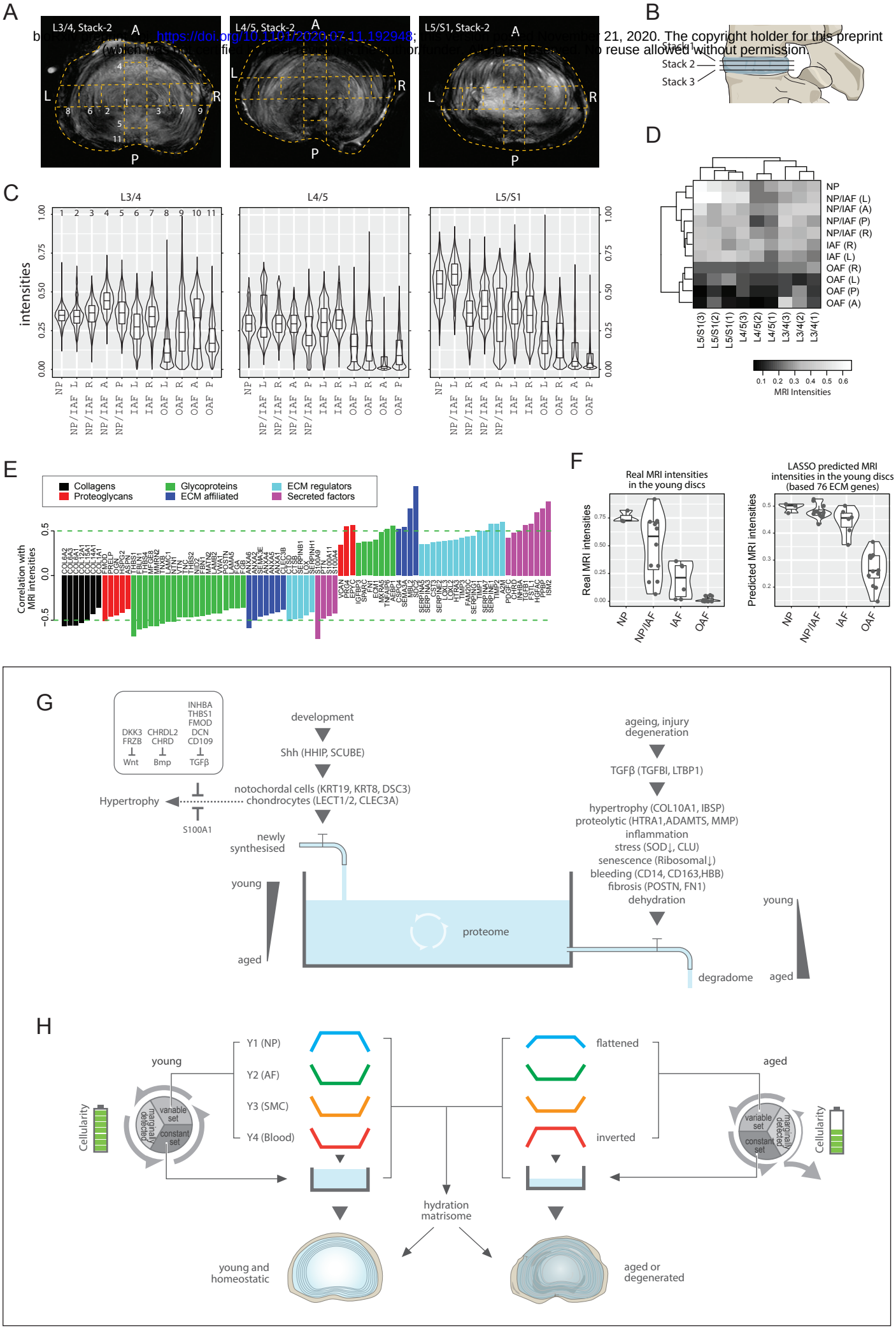
https://doi.org/10.1101/2020.07.11.192948; 21, 2020. The copyright holder for this preprint reuse allowed without permission.